Chapter 6

NUMERICAL MODELING OF EXTERNAL SULFATE ATTACK ON SATURATED CONCRETE SPECIMENS

Chapter 5 included a review of the most salient features concerning the experimental evidence on sulfate attack, together with a critical description of the relevant existing models. In this chapter, the model developed for the chemo-transport analysis used throughout this work is described in detail. It is based on the formulation proposed by Mobasher and coworkers (Tixier & Mobasher, 2003), with the addition of some refinements and the modification of specific features in the formulation. The present model additionally introduces the effect of cracks on the transport process in an explicit way. Several simulations with the aim of verifying the model implementation and its behavior in simple cases have been carried out. Next, the main results obtained concerning the coupled and uncoupled analyses of concrete specimens at the meso-level are presented and discussed, and possible future model enhancements are suggested.

6.1. External sulfate attack: model description

The coupled chemo-mechanical constitutive model developed and implemented in this thesis is based on the formulation proposed by Mobasher and coworkers (Tixier & Mobasher, 2003; Tixier, 2000) already described in Chapter 5 (section 5.2.2.2.), which has been modified by the introduction of some refinements. It consists of a single-ion diffusion-reaction model and considers a simplified view of the problem. Given the complexity of the real process, those authors assumed that external sulfate attack can be analyzed with only one diffusing ion type, represented by the ingressing sulfates, that then react with portlandite to form gypsum, and that the resulting gypsum reacts in turn with calcium alumina phases to form ettringite. The ettringite formed in this way is ultimately assumed to generate the volume expansions and be responsible for potential deleterious effects on the overall concrete composite. In this thesis, the original description and modeling of those diffusion/reaction processes has been improved. Also, as a second step, the model has been combined with the meso-mechanical model described in Chapter 2, in the context of a coupled approach, in order to study the chemo-mechanical degradation of concrete considering a random aggregate distribution and the cracking process explicitly. In addition, the effect of cracks on the transport process is accounted for. To the author's knowledge, the model described in this work is the only one currently capable of performing simulations at the meso-scale, i.e. explicitly considering the main heterogeneities of the material and the effect of cracking in the degradation process.

6.1.1. Chemical reactions considered and transport model

It is assumed that the ingressing sulfates first react with portlandite to form gypsum ($C\bar{S}H_2$), following equation 5.10 (alternatively, gypsum may be formed from the degradation of CSH). Thereafter, ingressing sulfates react with the different non-diffusing alumina phases of the HCP to form ettringite, as in equation 5.11. An additional reaction, not considered in the original model by Tixier & Mobasher, may be added to consider the formation of secondary ettringite from the alumino-ferrite phase (C_4AF) yielding a total of four possible reactions:

$$\begin{aligned}
&C_4AH_{13} + 3C\bar{S}H_2 + 14H \rightarrow C_6A\bar{S}_3H_{32} + CH \\
&C_4A\bar{S}H_{12} + 2C\bar{S}H_2 + 16H \rightarrow C_6A\bar{S}_3H_{32} \\
&C_3A + 3C\bar{S}H_2 + 26H \rightarrow C_6A\bar{S}_3H_{32} \\
&3C_4AF + 12C\bar{S}H_2 + xH \rightarrow 4\left(C_6A\bar{S}_3H_{32}\right) + 2\left[(A,F)H_3\right]
\end{aligned} \tag{6.1}$$

The following step in the model by Tixier & Mobasher was to consider a lumped reaction (eq. 5.12) in order to simplify the analysis. This implies the use of a single reaction rate coefficient for all the compounds (coefficient k in eqs. 5.13 and 5.14), meaning that the kinetics is the same for all reactions. In the present model it is proposed to optionally treat the reactions separately, thus allowing the consideration of different kinetics for each reaction individually (e.g. C_4AF is known to have slower reaction kinetics, see Schmidt, 2007).

The preceding chemical reactions take place according to the sulfates and calcium aluminates availability, which is determined in time and space through a second order diffusion-reaction equation for the sulfate concentration (denoted as U[mol/m^3 of material]) and additional equations for the depletion of the different *i* calcium aluminate phases (denoted as C_i[mol/m^3 of material]):

$$\frac{\partial U}{\partial t} = \frac{\partial}{\partial x}\left(D_U \frac{\partial U}{\partial x}\right) - U \cdot \sum_{i=1}^{n} k_i C_i \tag{6.2}$$

$$\frac{\partial C_i}{\partial t} = - k_i \frac{U C_i}{a_i} \qquad \text{for } i = 1,n \tag{6.3}$$

in which D_U [m^2/s] is the diffusion coefficient, k_i[m^3/(mol.s)] are the rates of take-up of sulfates, a_i are the stoichiometric coefficients for sulfates (in the form of gypsum) of the individual reactions and t[s] and x[m] are the time and space coordinate, respectively.

The consideration of different kinetics for each reaction adds (n-1) equations to the system. Fortunately, this poses no mathematical difficulty, since in the particular case of the implementation into a FE code, the variables C_i are considered as internal variables (defined at the integration points) and only the sulfate concentration is considered as nodal variable. Accordingly, for each iteration *j* of the solution strategy of the nonlinear system of eqs. 6.2 and 6.3, the *i* calcium aluminate phase for the next iteration (C_i^{j+1}) may be explicitly integrated as

$$C_i^{j+1} = C_i^j \cdot \exp\left\{-\frac{k_i}{a_i} \cdot \left(U^j + \Omega \cdot \Delta U^j\right) \cdot \Delta t\right\} \tag{6.4}$$

where Ω is the coefficient for time integration and Δt is $t^{j+1} - t^{j}$ (see Appendix A for derivation of eq. 6.4).

Note: In this version of the model, the proportions of the different aluminate phases (relative to each other) need not to remain constant throughout the simulation, but will generally depend on the difference between the rates of reaction k_i.

However, the kinetics of the individual reactions on the formation of ettringite is often not known *a priori* and the above reactions (eq. 6.1) may be advantageously lumped into one single expression as

$$CA + q\bar{S} \rightarrow C_6A\bar{S}_3H_{32} \tag{6.5}$$

where $CA = \gamma_1 C_4AH_{13} + \gamma_2 C_4A\bar{S}H_{12} + \gamma_3 C_3A + \gamma_4 C_4AF$, and $q = 3\gamma_1 + 2\gamma_2 + 3\gamma_3 + 4\gamma_4$ represents the stoichiometric weighted coefficient of the sulfate phase and γ_i is the proportion of each aluminate phase, calculated as

$$\gamma_i = \frac{C_i}{\sum_{i=1}^{4} C_i} \tag{6.6}$$

in which C_i[mol/m^3 of material] represents the molar concentration of each aluminate phase per unit volume of solid material. Note that γ_i is variable only if different reaction kinetics are considered (otherwise it remains constant in time).

By introducing this lumped reaction, eqs. 6.2 and 6.3 may be rewritten as follows

$$\frac{\partial U}{\partial t} = \frac{\partial}{\partial x}\left(D_U \frac{\partial U}{\partial x} \right) - kUC \tag{6.7}$$

$$\frac{\partial C}{\partial t} = - k \frac{UC}{q} \tag{6.8}$$

where C[mol/m^3 of material] represents now the equivalent lumped reacting calcium aluminates (CA in eq. 6.5) and k[m^3/(mol.s)] is the lumped rate of take-up of sulfates, to be determined by inverse analysis. Note that the model in this simplified version needs to calculate and store only one internal variable per integration point.

6.1.2. Diffusion coefficient for sulfate ions: uncracked porous medium

An important difference with respect to the model proposed by Tixier & Mobasher consists in the variation of the diffusion coefficient, which in this work is assumed to be dependent on the pore filling effect (the diffusivity decreases as pores are filled with precipitated species). The original proposal considered only the increase of the diffusion coefficient with microcracking through a damage variable (Tixier, 2000). It should be noticed that in our model diffusion through the cracks is explicitly considered with the introduction of zero-thickness interface elements. In this way, the model accounts for the decrease in diffusivity due to the pore filling effect simultaneously with an increase of the effective overall diffusivity due to cracking phenomena.

Different models have been proposed to introduce the pore filling effect (see Garboczi & Bentz, 1992; Gospodinov *et al.*, 1996; Lagneau, 2000; Samson & Marchand, 2007). For instance, models for ionic transport in groundwater traditionally use a modified version of the Kozeny-Carman relationship which may be written as

$$D_{\Phi}\left(\Phi_{cap}\right)=\left(\frac{\Phi_{cap}}{\Phi_{ini}}\right)^{3}\left(\frac{1-\Phi_{ini}}{1-\Phi_{cap}}\right)^{2} \tag{6.9}$$

in which Φ_{ini} is the initial capillary porosity and Φ_{cap} represents its updated value, i.e. considering the change in porosity due to precipitation of secondary species. More recently, an expression developed for cementitious materials has been proposed as (Samson & Marchand, 2007):

$$D_{\Phi}\left(\Phi_{cap}\right)=e^{4.3\Phi_{cap}/V_P}\cdot e^{-4.3\Phi_{ini}/V_P}\cdot D_0 \tag{6.10}$$

where D_0 is a reference value, V_P is the paste volume of the material [m^3/m^3 of material] and Φ_{cap} is calculated as

$$\Phi_{cap}=\Phi_{ini}+\sum_{i=1}^{m}\left(V_i^{ini}-V_i\right) \tag{6.11}$$

where V_i is the volume of a given solid phase [m^3/m^3 of material], and m is the total number of solid phases. Unfortunately, the diffusion coefficient calculated with this relationship does not depend on the initial capillary porosity, which is an essential feature:

$$D_{\Phi}\left(\Phi_{cap}\right)=D_0\frac{e^{4.3/V_P\cdot\left(\Phi_{ini}+\sum_{i=1}^{m}\left(V_i^{ini}-V_i\right)\right)}}{e^{4.3\Phi_{ini}/V_P}} \tag{6.12}$$

which may be rewritten as

$$D_{\Phi}\left(\Phi_{cap}\right)=D_0e^{4.3/V_P\cdot\left(\Phi_{ini}+\sum_{i=1}^{m}\left(V_i^{ini}-V_i\right)\right)-4.3/V_P\cdot\Phi_{ini}}=D_0e^{4.3/V_P\cdot\sum_{i=1}^{m}\left(V_i^{ini}-V_i\right)} \tag{6.13}$$

To overcome this drawback, in the present model a hyperbolic function similar to the analysis of moisture diffusivity (described in Chapter 4) has been adopted, which yields comparable trends to the relationship proposed by Samson & Marchand (2007). Accordingly, the diffusion coefficient is calculated as

$$D_{\Phi}\left(\Phi_{cap}\right)=D_0+\left(D_1-D_0\right)f\left(\beta_D,\Phi_{cap}\right) \tag{6.14}$$

where $f\left(\beta_D,\Phi_{cap}\right)=\frac{e^{-\beta_D}\xi}{1+\left(e^{-\beta_D}-1\right)\xi}$, with $\xi=\left(\Phi_{cap}/\Phi_{ini}\right)$ (6.15)

A comparison between different models proposed in the literature, some of them mentioned above, and the hyperbolic expression proposed in this thesis is shown in figure 6.1. Note that with the use of eq. 6.14 the pore clogging (obstruction of capillary pores) does not necessarily yield a zero diffusion coefficient, as in the proposals by Kozeny-Carman or Gospodinov *et al.* (1996). Instead, it depends on the value of D_0 adopted. This implies that a part of the diffusion process may occur through the gel pores (nano-pores), which have been suggested to be interconnected (Stora, 2007). The initial capillary porosity is calculated through a Powers' model (eq. 6.16) and the updated value considers the growth of ettringite in the pores through eq. 6.17:

$$\Phi_{ini}=v_c\cdot\left(\frac{w/c-0.36\alpha}{w/c+0.32}\right),\ \text{if}\ w/c>0.36\alpha\ \text{(and 0 otherwise)} \tag{6.16}$$

$$\Phi_{cap} = \Phi_{ini} - \alpha_s CA^{react} \text{, if } \alpha_s CA^{react} < \Phi_{ini} \text{ (and 0 otherwise)} \quad (6.17)$$

where v_c [m^3/m^3 of material] is the volumetric fraction of cement in the solid, w/c is the water cement ratio, α the degree of hydration and α_s and CA^{react} are defined in the following.

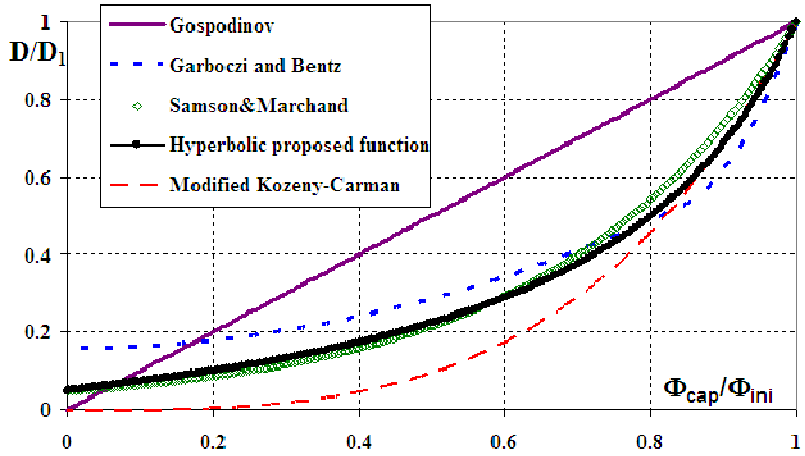

Figure 6.1. Comparison between different models found in the literature for calculating the diffusion coefficient and the model proposed in this work (for β_D = 1.5): normalized diffusion coefficient vs. normalized capillary porosity.

6.1.3. Diffusion of sulfate ions through the cracks

Similar to the case of moisture diffusion, the effect of cracks on the transport of sulfate ions is explicitly considered in the model *via* the introduction of zero-thickness interface elements. This effect may be of importance for determining penetration fronts in a more accurate way. Moreover, in the cases where spalling occurs, a drastic change in the boundary conditions of the chemo-transport analysis is expected to take place, thus accelerating the degradation process. Nevertheless, this important feature has not been given a lot of attention in the models proposed so far, mainly due to the complexity of introducing this aspect in the calculations and also due to the fact that the existing models do not predict the crack patterns and the spalling effect accurately.

Analogously to the case of moisture diffusion through the cracks (described in Chapter 4), a relationship between crack width and diffusivity must be introduced. In this regard, recent experiments have been carried out elsewhere in concrete samples to determine the diffusivity of chloride ions through cracked concrete (Djerbi *et al.*, 2008, see also section 3.1.5 in Chapter 3). With the setup of a classical chloride migration test (shown in figure 6.2a), but artificially producing traversing cracks in the samples through an indirect tensile test (samples were cylindrical), they concluded that the relationship between diffusivity and crack opening is linear, at least until a threshold of around 100 microns is attained for the crack width, after which it remains constant and approximately equal to the diffusivity in free solution (around $1.2x10^{-9}$[m^2/s], for chloride ions). In order to derive this relationship, they assumed a decomposition of the total chloride diffusion flux (J_t[mol/(m^2.s)]) into a flux through the uncracked specimen (J_0[mol/(m^2.s)]), with a transversal area A[m^2], and a flux in the crack (J_{cr}[mol/(m^2.s)]), with an area A_{cr}[m^2], which can be computed knowing the crack opening, yielding (Gérard & Marchand, 2000)

$$\left(A+A_{cr}\right)J_t = AJ_0 + A_{cr}J_{cr} \tag{6.18}$$

with $J_t = BD$, $J_0 = BD_0$ and $J_{cr} = BD_{cr}$ (6.19)

Parameter B is a constant of the test, depending on the specimen thickness, the imposed potential drop between the specimen surfaces and the chloride concentration upstream. D[m^2/s] and D_0[m^2/s] are the diffusion coefficients of the cracked and uncracked specimens, respectively, and D_{cr}[m^2/s] is the diffusivity of the crack. In this way, the previous equation may be rewritten to calculate the diffusion coefficient in the crack, yielding:

$$D_{cr} = \left[A\left(D - D_0\right) + A_{cr}D\right]\cdot\left(A_{cr}\right)^{-1} \tag{6.20}$$

Equation 6.20 is plotted in figure 6.2b as a function of the crack width, showing a linear relation until a threshold is reached, after which it remains at a constant value. This threshold coincides approximately with the diffusion coefficient of chlorides in free solution. The total flux is given by the slope of the curve relating chloride concentration downstream and time, which is shown in figure 6.2c. As the crack width increases the total flux also increases due to the increase not only of J_{cr}, but also in A_{cr} (note that the flux increases even for crack widths beyond the critical crack opening).

For the implementation of the above relation within the framework presented in Chapter 4 (expressions 4.6 to 4.9), coefficient D_{cr} [cm^2/s] (equivalent to K_L [cm^2/s] in eq. 4.7) is multiplied by the crack width $u{\cdot}D_{cr}$ (u being the crack opening), in order to relate the total transport through a discontinuity with the concentration gradient. As a result, a quadratic law of the diffusivity in terms of the crack width is obtained, until the threshold crack opening is reached, after which the diffusion coefficient increases linearly with crack width, as shown in figure 6.3.

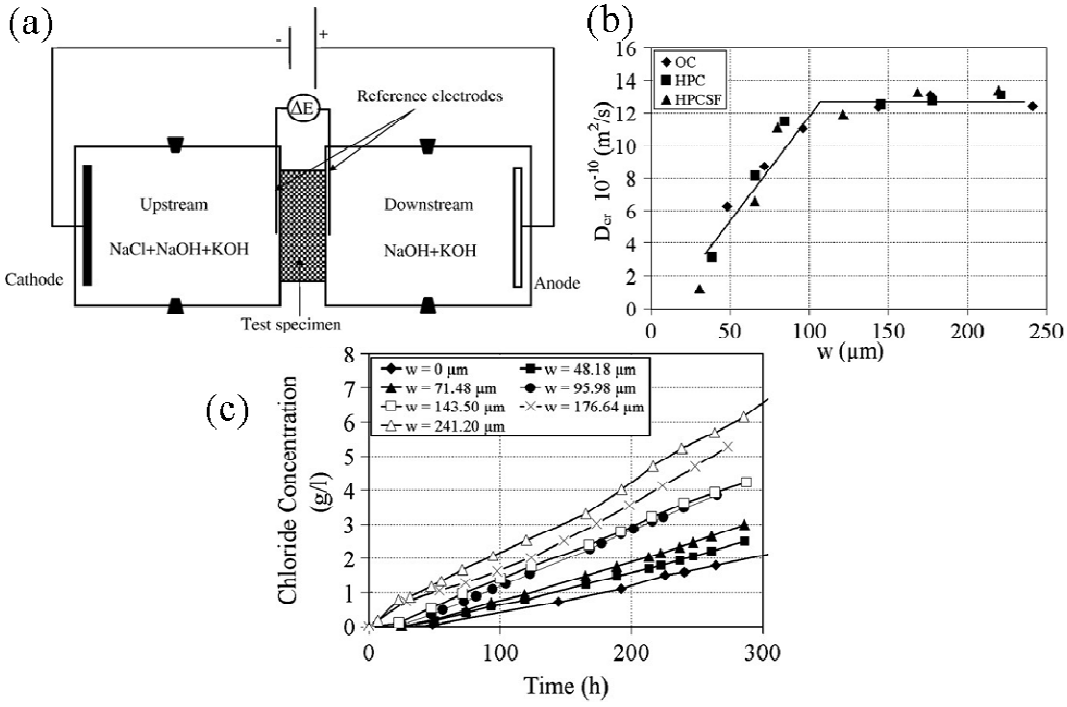

Figure 6.2. Estimation of the effect of the width of a crack on its diffusivity: (a) migration test setup; (b) relation between diffusion through the crack and crack opening; (c) variation of the downstream concentration with time (from Djerbi *et al.*, 2008).

There seems to be no such a study for the diffusion of sulfate ions through cracked concrete specimens, although it could be expected that the main conclusions drawn for the chlorides diffusion are applicable to the sulfates case, since the diffusivities in free solution are similar for both types of ions (around $1.2x10^{-9}$[m^2/s] for chloride ions and $1x10^{-9}$[m^2/s] for sulfate ions SO_4^{2-}, see Samson *et al.*, 2003). However, more research would be needed to confirm these findings.

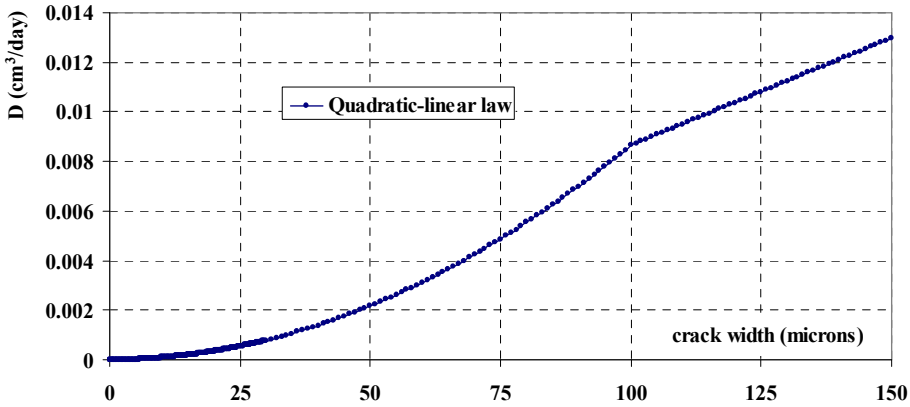

Figure 6.3. Relation between the diffusion coefficient for the zero-thickness interface elements and the crack opening to be used in the simulations.

In the present model, as a first approximation, the above described quadratic-linear relation between the diffusivity for the interface elements and the crack width has been implemented. In addition, the cubic law (described in Chapter 4) has also been considered as an option, and a comparison between the two possibilities has been carried out (see section 6.3.3.).

In order to derive the quadratic-linear law, it is assumed that the diffusivity increases with the square of the crack width, between the values zero (for a closed crack) and a critical crack aperture, u_{crit}, of 100 microns. For larger crack openings, the diffusivity through the crack is considered to be proportional to the crack width, the slope being the diffusion coefficient in free water. This yields the following relationship between crack opening and diffusivity:

$$K_L(u) = \kappa \cdot u^2, \text{ if } u < u_{crit} = 100\mu\text{m} \tag{6.21}$$

$$K_L(u) = \kappa \cdot u_{crit} \cdot u, \text{ if } u \geq u_{crit} \tag{..(6.22)}$$

$$\text{with } \kappa \cong \frac{D_{free} - 0}{u_{crit} - 0} = \frac{1x10^{-9}\,\text{m}^2/\text{s}}{100\mu\text{m}} = 10^{-5}\,[\text{m/s}] \tag{6.23}$$

6.1.4. Calculation of volumetric expansions

Ettringite is assumed to be the only reaction product governing the expansion of the sample. The volumetric strain (ε_v) is obtained from the amount of reacted calcium aluminate and the volume change associated with it. For any of the individual reactions described above, the volumetric change due to the difference in specific gravity can be calculated using stoichiometric constants (Tixier & Mobasher, 2003):

$$\frac{\Delta V_i}{V_i} = \frac{m^{ettr}}{m_i + a \cdot m^{gypsum}} - 1 \tag{6.24}$$

in which m^i is the molar volume [m^3/mol] of each species and a is the stoichiometric coefficient involved in the reaction. For calculating the total volumetric strain, it is necessary to compute the amount of aluminate phases that have reacted (CA^{react} in the case of the lumped reaction and C_i^{react} for the extended model).

In the case that the extended version of the model is used, the volumetric strain is calculated as follows

$$\varepsilon_v = \sum_{i=1}^{n} C_i^{react} \frac{\Delta V_i}{V_i} m_i - f \cdot \Phi_{ini} \tag{6.25}$$

with $C_i^{react} = C_i^0 - C_i^{unr}$, for i = 1, n (6.26)

In the previous equations, C_i^0 represents the initial concentration of the different alumina phases and C_i^{unr} is the amount of each of the unreacted aluminates (given by the updated values of the internal variables), Φ_{ini} is the initial capillary porosity (estimated through a Powers' type model) and f is the fraction of capillary porosity that has to be filled before any expansion occurs.

For the simplified model, an averaging scheme is again used for the different phases (Tixier & Mobasher, 2003), yielding

$$\varepsilon_v = \alpha_s \cdot CA^{react} - f \cdot \Phi_{ini} \tag{6.27}$$

with $\alpha_s = \sum_{i=1}^{n} \frac{\Delta V_i}{V_i} \cdot m_i \cdot \frac{C_i}{\sum_j C_j}$ (6.28)

Typical values of the parameter f in the second term of the RHS of eq. 6.27 (threshold term) are in the range 0.05-0.40 (see Tixier & Mobasher, 2003). The scarcity and the low range of the values needed to fit experimental data suggest that the assumption that a fraction of the capillary porosity has to be filled before any expansion is observed may be rather arbitrary and could be therefore questionable.

In marked contrast, it has recently been suggested that ettringite crystals precipitate not only in the capillary pores, but also within the CSH phase (in the so-called gel porosity), as in the case of delayed ettringite formation (Taylor *et al.*, 2001; Scrivener, 2008). This hypothesis considers that the main cause of expansions is the ettringite precipitation within the CSH phase, and that the part that precipitates within the capillary pores does not have a significant contribution to the overall expansion.

The evolution in time of the proportions of the ettringite that precipitates within the CSH and in the pores is at present not known, not even for the final state of the sample (which is typically the state at which the samples are analyzed). In fact, it is not expected that this proportion remains constant in time, since the system thermodynamically favors the formation of ettringite crystals in larger (capillary) pores, thus reducing the crystallization pressure exerted to the solid and the consequent expansions (Flatt & Scherer, 2008). However, the dissolution of ettringite in smaller pores and its subsequent migration and recrystallization into larger pores is not an instantaneous process, but is limited by the diffusion of ions at the microscale. As a result, it is expected that expansions can occur without ettringite having to fill all large pores, as observed in the experiments. This process depends on many factors, like the level of constraint of ettringite crystals, the supersaturation of the pore solution, the

spatial distribution of the reacting aluminate phases, and the pore size distribution (Flatt & Scherer, 2008).

Although this hypothesis is different from the one adopted in most of the models proposed so far, including the one presented in this thesis, the mathematical treatment in both cases may be similar, except that in the latter case the threshold term may not be a constant, as in the present model, but a complex function of the above mentioned factors (the pore size distribution has already been identified as an important factor, see Schimdt-Döhl & Rostásy, 1999). This fact could also have implications for the estimation of the diffusion coefficient through the continuum, since it generally depends on the available capillary porosity. Despite the previous considerations, and until a clearer idea of the mechanisms is generally accepted, it has been decided in this work to maintain the formulation given by the expressions 6.24 to 6.29.

6.2. First-stage verifications

6.2.1. Verification of the implementation of the model

The implementation of the sulfate attack model presented in the previous section into the FE code DRACFLOW has been verified with two simplified examples with analytical solution in 1D and 2D (from Tixier & Mobasher, 2003, solution extracted from Crank, 1956). The simplified differential equation solved analytically corresponds to the case in which C does not deplete (or, equivalently, that there is an unlimited supply of C) and is given by

$$\frac{\partial U}{\partial t} = \frac{\partial}{\partial x}\left(D_U \frac{\partial U}{\partial x} \right) - k' U \tag{6.29}$$

with D_U = constant. The solution to this differential equation for the case of an infinitely long slab of thickness L exposed to an initial sulfate concentration U_0 on both faces yields

$$\frac{U}{U_0} = 1 - \frac{4}{\pi} \sum_{m=0}^{\infty} \frac{1}{n\left(k' + \nu\right)} \sin\left(\frac{n\pi X}{L} \right) \left(k' + \nu \exp\left[-t\left(k' + \nu \right) \right] \right) \tag{6.30}$$

$$\text{with } \nu = D_U \left(\frac{n\pi}{L} \right)^2 \text{ and } n = 2m + 1 \tag{6.31}$$

In figure 6.4, the numerical results obtained with the two-dimensional FE discretization of the 1D problem are compared with the analytical solution (in 1D) for the following values of the parameters (as in Tixier & Mobasher, 2003): $D_U = 10^{-12}$ m^2/s, L = 25mm and $k' = 10^{-8}$ s^{-1}. Figure 6.4a shows the distribution over the slab thickness of the normalized concentration of sulfates for three different exposure times (145, 434 and 723 days). Figure 6.4b presents the comparison of numerical and analytical curves of the available normalized concentration of sulfates over the semi-thickness of the slab for the same three exposure times, showing a very good agreement. It can be observed that, for a given distance to the exposure surface, the concentration of sulfates increases with time. However, the concentration is lower than that obtained in a pure diffusion analysis (Fick's law, with k =0) with the same parameters (not included in the figure), due to the presence of a sink term representing the reactions.

Figure 6.5 shows the results of a similar comparison between a simulation and the analytical solution, only that in this case a 2D squared slab exposed in all the four surfaces is considered, again with a very good agreement.

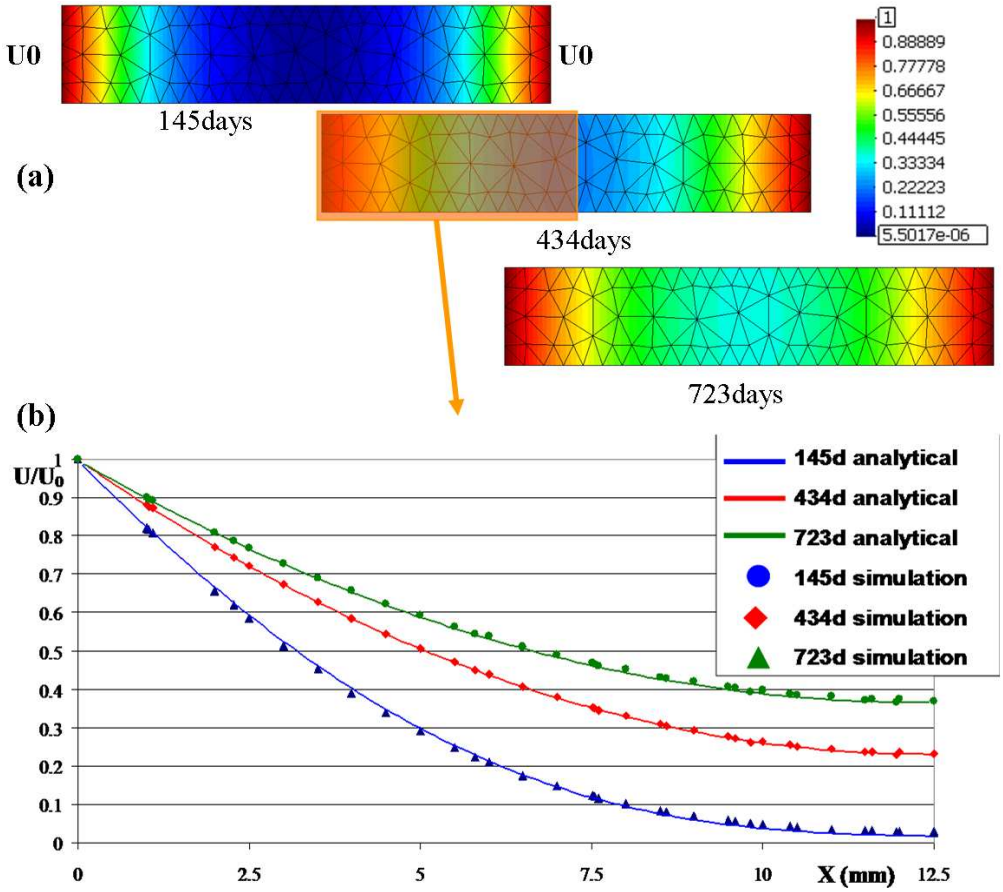

Figure 6.4. Verification example in 1D of the diffusion-reaction formulation for sulfate attack with first order kinetics (not considering C). (a) Normalized sulfates distribution across the thickness L of the slab, and (b) comparison between numerical and analytical solutions of normalized sulfate curves over the semi-thickness of the slab.

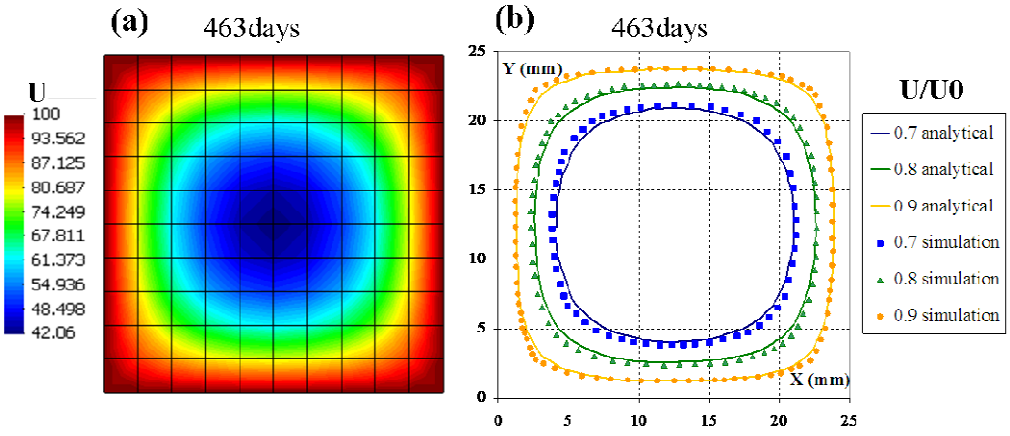

Figure 6.5. 2D Verification example of the diffusion-reaction formulation for sulfate attack with first order kinetics (not considering C): (a) FE solution for the sulfates distribution in a squared slab of size L for an exposure time of 463 days, and (b) comparison between numerical and analytical solutions of normalized sulfate iso-curves over slab surface at 463 days.

6.2.2. Macroscopic simulation of the expansion of mortar prisms

With the aim of determining the order of magnitude of the main parameters of the chemo-transport model for mortar, it was decided to simulate recent external sulfate attack experiments on mortar prisms at the macroscopic scale, i.e. considering the material as continuum and homogeneous. The experimental campaign was carried out at UPC (Akpinar, 2006), following ASTM C1012 test method ($25x25x285mm^3$ mortar prisms immersed in 5% Na_2SO_4 solution). Among other test variables, the influence of the initial C_3A content in the cement was studied by testing two mortars made from CEM I 52.5R (9.13wt% C_3A) and CEM I 52.5N/SR (4.56wt% C_3A) cements, which have been chosen for the simulations.

Simulations of expansions were performed in 3D considering three symmetry planes (as shown in figure 6.7a), and assuming as a first approximation a linear elastic behavior. Although this may imply an oversimplification of the material response, since no microcracking and other nonlinearities are considered, results may be useful for determining rough values for the input parameters of the chemo-transport model. Moreover, the experimental tests have not reached a considerable state of degradation during the exposure time, with spalling of mortar layers or complete disintegration of the sample, as shown in figure 6.6 (Akpinar, 2009). Only the onset of cracking has been attained at that exposure time. The material parameters finally used to fit the experimental measurements are summarized in table 6.1. Boundary conditions consist of imposing a constant sodium sulfate concentration in the outer surfaces and no flux is allowed through the symmetry planes.

	Mortar made from CEM I 52.5N/SR	Mortar made from CEM I 52.5R
$D(mm^2/day)$	$2x10^{-3}$	$1.7x10^{-1}$
$k(m^3/(mol.day))$	$9x10^{-5}$	$8x10^{-5}$
q	3	3
α_s	$1.13x10^{-4}$	$1.13x10^{-4}$
$f\Phi$	$4x10^{-4}$	$2x10^{-3}$
E(Gpa); ν	27; 0.2	27; 0.2
Boundary conditions	35.20 Na_2SO_4 (mol/m^3)	35.20 Na_2SO_4 (mol/m^3)

Table 6.1. Material parameters and boundary conditions used to fit the experimental results by Akpinar (2006).

Figure 6.7a shows the ettringite distribution obtained in the simulations at 1,000 days of exposure. In figure 6.7b it can be seen that the predicted penetration front of ettringite precipitation is higher in the case of high C_3A content, in comparison with the low one, at 2,000 days of exposure. The results of the simulations of the low and high C_3A mortars, in terms of expansions *vs.* the exposure time, are compared with the experimental measurements in figure 6.8, showing a good agreement.

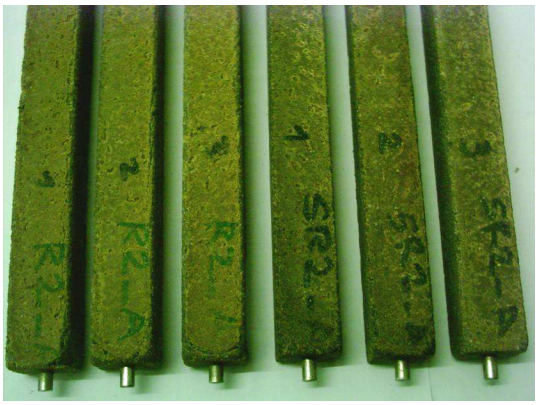

Figure 6.6. Photograph of the mortars made from CEM I 52.5R (9.13wt% C_3A, marked as R2) and CEM I 52.5N/SR (4.56wt% C_3A, marked as SR2) cements, after 68 weeks of exposure to 5% sodium sulfate solution (Akpinar, 2009).

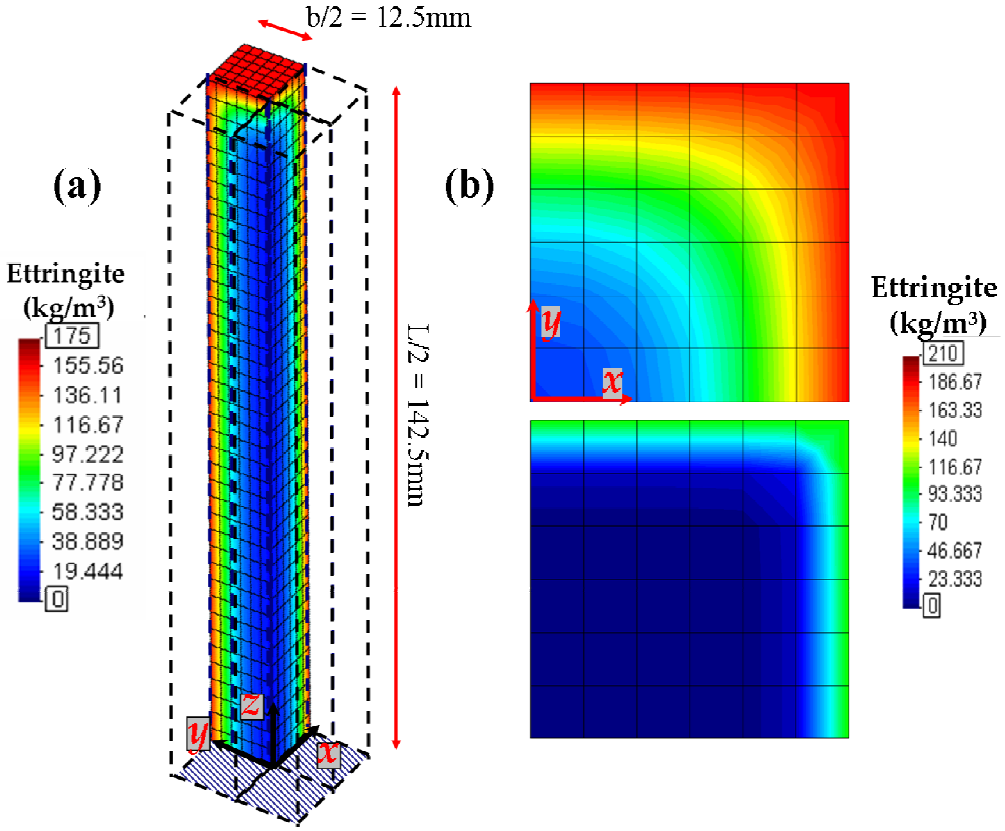

Figure 6.7. Ettringite distribution (a) in the 3D mesh for the case of 9.13% wt. C_3A at 1,000 days of exposure, and (b) in the middle cross-section (at L/2) for the low (bottom) and high (top) C_3A content cases, at 2,000 days of exposure.

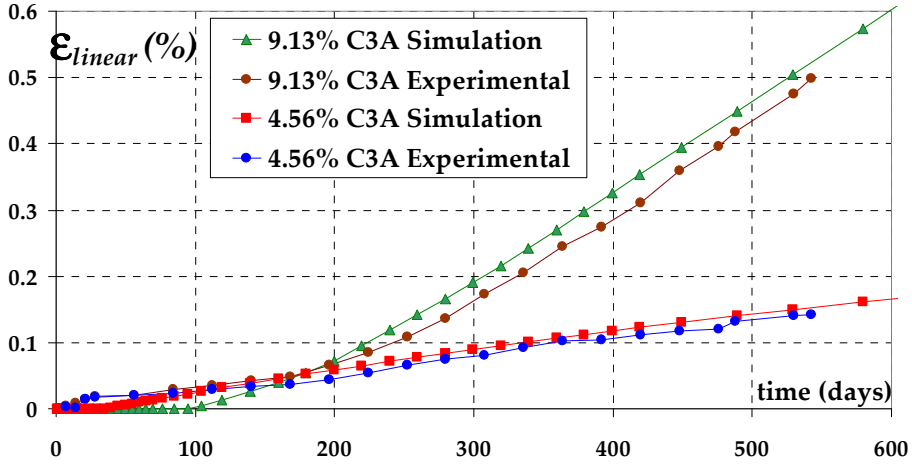

Figure 6.8. Comparison of the evolution of expansions obtained in the simulations and observed experimentally in the two types of mortar studied.

6.2.3. Effect of a single inclusion on the cracking due to matrix expansion

Prior to the study at the mesoscale of the expansive reactions related with the external sulfate attack process in concrete, some preliminary calculations on the influence of the aggregate size on the cracks induced by an arbitrary uniform matrix expansion have been carried out. The same meshes with 2, 4 and 6cm aggregates and identical material parameters as in Chapter 4 (section 4.5.1.) have been used for the simulations (figure 4.25). The only difference is that in this case a uniform volumetric expansion of the matrix phase was incrementally imposed. This problem has been previously studied with linear elastic theory and analytical solutions (Goltermann, 1994; Garboczi, 1997). Due to the expansion of the matrix, a gap between the matrix and the aggregate is formed. The tangential stress is always compressive in the matrix, so that no radial cracking is expected. In case of considering the aggregate-matrix interface as a free boundary, it has been shown with elasticity theory that the width of the gap (u[cm]) around the aggregate is simply given by

$$u = \varepsilon \cdot a \tag{6.32}$$

where a is the aggregate radius [cm] and ε is the uniform volumetric expansion imposed in the matrix. Figure 6.9 presents the results of the simulations in terms of the deformed meshes for each of the three cases, where a gap between the matrix and the aggregate can be clearly observed. In figure 6.10a the width of the gap obtained in the three cases is compared to the analytical solution, showing a perfect agreement. Finally, the energy spent in the fracture process for the 6cm aggregate mesh is shown in figure 6.10b, confirming the lack of radial cracks.

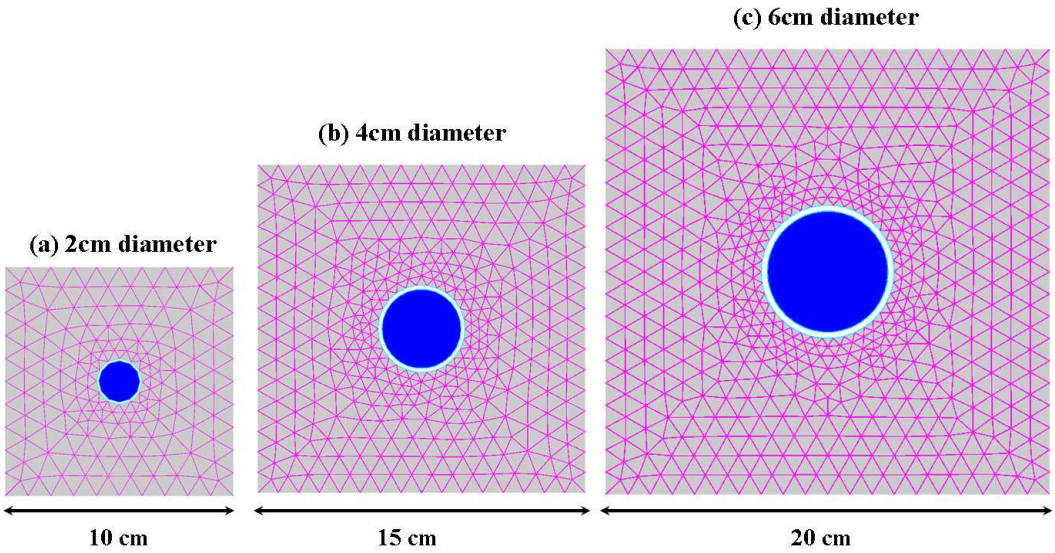

Figure 6.9. Deformed meshes (scale factor = 40) for the three cases analyzed, showing an increasing separation between the inclusion and the matrix with aggregate size.

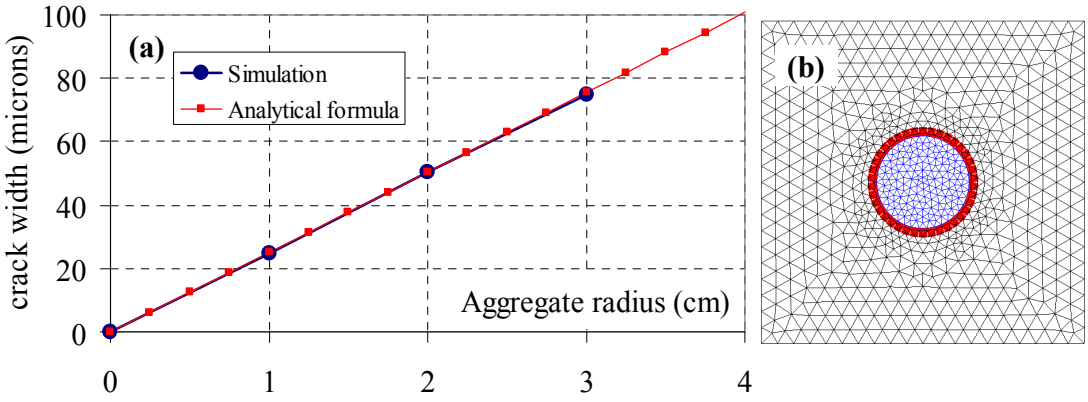

Figure 6.10. Effect of the size of a single inclusion on the expansion-induced cracking: (a) Analytical solution vs. simulation results; (b) energy spent in the fracture process around the 6cm inclusion.

6.3. Coupled chemo-mechanical (C-M) analysis at the meso-scale

Coupling between the diffusion-reaction and the mechanical analyses has been implemented by the staggered approach already described in Chapter 4, using the same FE mesh for both calculations.

First, an academic simulation of external sulfate attack over a small concrete specimen with a cross-section of 6*x*6cm^2 and a 4*x*4 aggregate arrangement (26% volume fraction and 15mm of maximum aggregate size) has been studied (figure 6.11). The four edges of the specimen are exposed to a sodium sulfate solution with a fixed concentration (U_{imp}) of 35.2 [mol/m^3], equivalent to a 5% Na_2SO_4 solution. The single lumped reaction version of the model, with a single history variable, has been used in this case, and the variable diffusivity according to eq. 6.14 has been considered. For the matrix phase, a concentration of 4.56 (low) or 9.13 (high) wt. % of C_3A (weight of the cement), depending on the case, has been used in the simulations (knowing the cement content of the matrix phase, an initial concentration of C_3A [mol/m^3] can be derived, see section 6.3.2.). These concentrations correspond to a CEM I 52.5N/SR (sulfate-resistant cement) and a CEM I 52.5R cement, respectively. The rest of the material parameters

for the diffusion-reaction analysis are as follows: D_0 = 1.96x10^{-12} [m^2/s], k = 0.92x10^{-9} [m^3/(mol.s)], q = 3, f = 0.05, w/c = 0.5, α = 0.9, D_0/D_1 = 0.2, β_D = 1.5 and α_s = 1.133x10^{-4}. The effect of cracks on the sulfate ions diffusion is considered in the coupled simulations with the introduction of zero-thickness interface elements and assuming the validity of the cubic law, with a parameter high enough to ensure a much more rapid diffusion through the crack than through the uncracked continuous medium. Finally, the model parameters for the mechanical analysis, without considering the aging effect and the viscoelastic behavior in this first stage, are the following: E_{aggr} = 70,000MPa (aggregate elastic modulus), E_{matrix} = 25,000MPa (matrix elastic modulus), ν = 0,20 (Poisson coefficient for both continuum phases); for the aggregate-matrix interface elements:χ_0 = 2MPa, c_0 = 7MPa, tanϕ_0 = 0.7, tanϕ_r = 0.4, G_F^I = 0.03 N/mm, G_F^{IIa} = 10·G_F^I, σ_{dil} = 40 MPa; for the matrix-matrix joint elements: same parameters, except χ_0 = 4MPa, c_0 = 14MPa, G_F^I = 0.06 N/mm, G_F^{IIa} = 10·G_F^I.

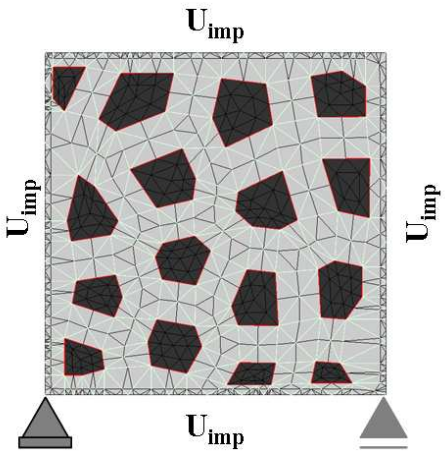

Figure 6.11. Mesh used in the simulations.

6.3.1. Comparison between coupled and uncoupled analyses

In order to verify the model response when cracking occurs, coupled and uncoupled simulations have been performed over the same FE mesh, for the case of high C_3A content (9.13 wt. %). Figure 6.12 depicts the results of the evolution of ettringite concentration [kg/m^3] for the (a) uncoupled and (b) coupled cases, and for three different advanced exposure times (all after appreciable differences are observed between the two types of calculations). It may be noted that the front of ettringite formation, as a consequence of the penetration of the sulfate ions, advances with time towards the center of the specimen in a much more accelerated way for the coupled case, once cracking and spalling develop.

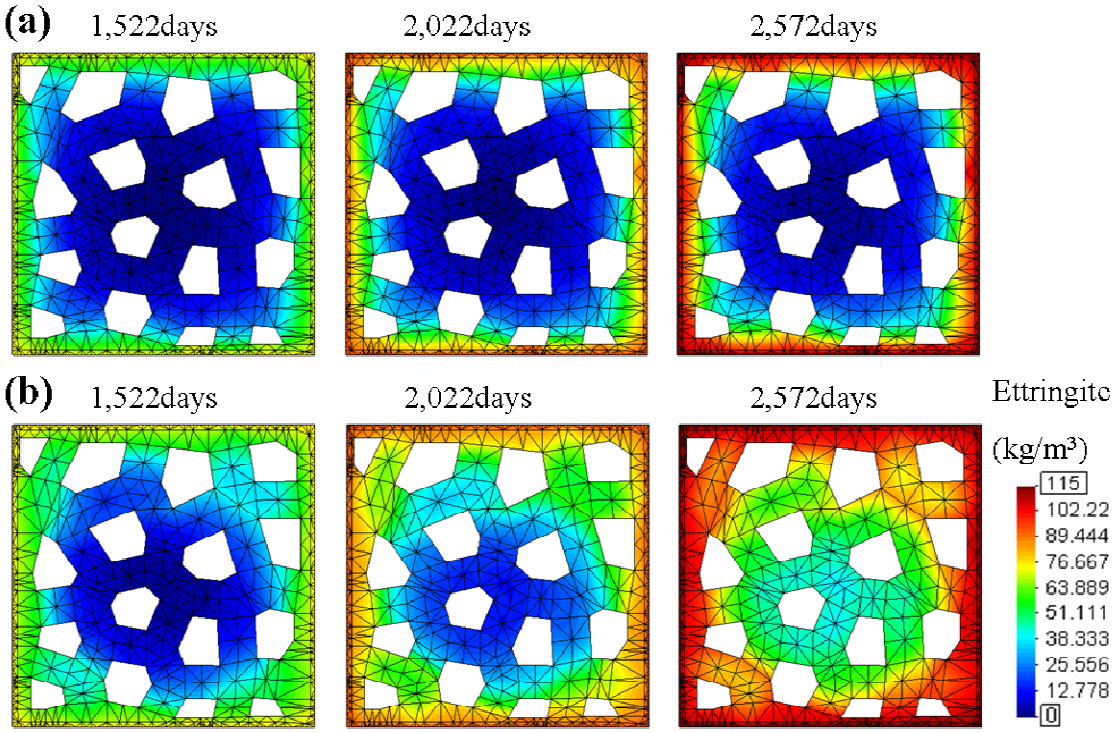

Figure 6.12. Comparison of the evolution in time of the concentration of ettringite [kg/m^3], for: (a) uncoupled and (b) coupled cases, at t = 1,522, 2,022 and 2,572 days.

In turn, figure 6.13 illustrates the evolution of the crack pattern, in terms of the energy spent in the fracture process, for four different exposure times. The open cracks (that have reached the initial cracking surface) are highlighted, in red if they are opening (plastic loading) or in blue if they are arrested (elastic unloading). The thickness of the color line represents the energy spent at each point. It can be seen that cracking begins at the specimen corners, in the aggregate-matrix interfaces (figure 6.13a). These cracks evolve with time, get connected through matrix cracks and eventually produce the spalling of a mortar layer, approximately at 1,000 days of exposure, which can be seen in the figure as cracks parallel to the exposed surfaces, over the entire perimeter.

Figure 6.14 shows the evolution of the fracture process for the same exposure times of figure 6.12 and also for an earlier stage (722 days), for the (a) uncoupled and (b) coupled cases. A correlation between the results presented in figure 6.12, regarding the ettringite concentration, and the crack patterns shown in the latter figure, is clearly observed. At the moment in which the cracks at the corners connect with the exposed surfaces, the coupled simulation accentuates the influence of these cracks as preferential penetration channels, leading to an increase of the ettringite formation and thus on a higher level of expansions. In turn, a higher degree of internal microcracking between and around the aggregates is reached in the coupled case, in comparison with the uncoupled one. The maximum crack widths (located at the ring-shaped crack determining the spalling effect) at 2,572 days of exposure are of the order of 140 microns in the coupled case and 240 microns in the uncoupled one. The reason why the crack opening in the uncoupled analysis is larger than in the coupled case may be found in figure 6.15, where the ettringite concentration profiles at 2,572 days are plotted for the two cases. It can be seen that in the uncoupled analysis, due to the reduction of the diffusion coefficient and the fact that the effect of cracks is not considered in the diffusion process, the ettringite profile has a higher gradient near the exposed surfaces, thus causing excessive expansion of the outer layers and almost none in the interior of

the sample. This is not the case in the coupled simulation, which shows a non-negligible ettringite content also in the interior of the sample, thus producing a more homogeneous expansion of the specimen, as compared to the uncoupled simulation.

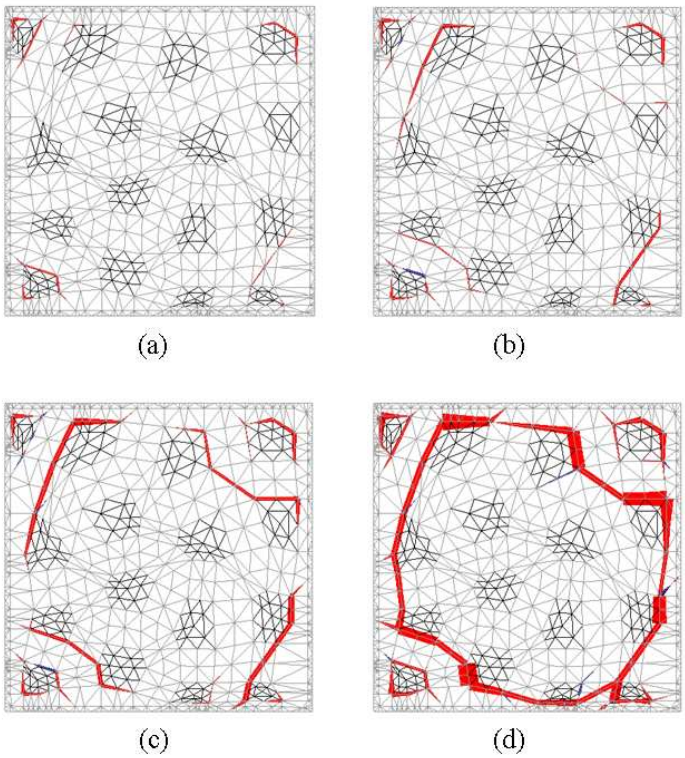

Figure 6.13. Crack pattern evolution, in terms of energy spent in the fracture process, for the following exposure times: (a) 672, (b) 722, (c) 772 and (d) 1,022 days (until this point the results of the coupled and uncoupled analyses are almost equivalent).

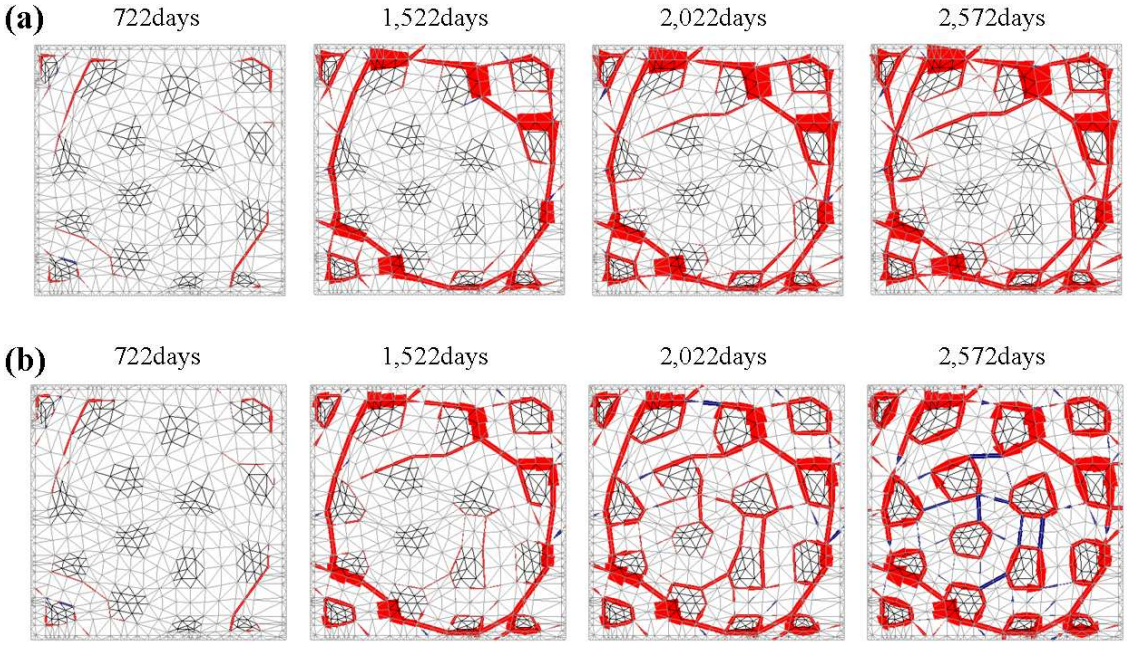

Figure 6.14. Crack pattern evolution in terms of energy spent in the fracture process, showing spalling and microcracking around the aggregates, for the (a) uncoupled and (b) coupled cases at exposure times of 722, 1,522, 2,022 and 2,572 days.

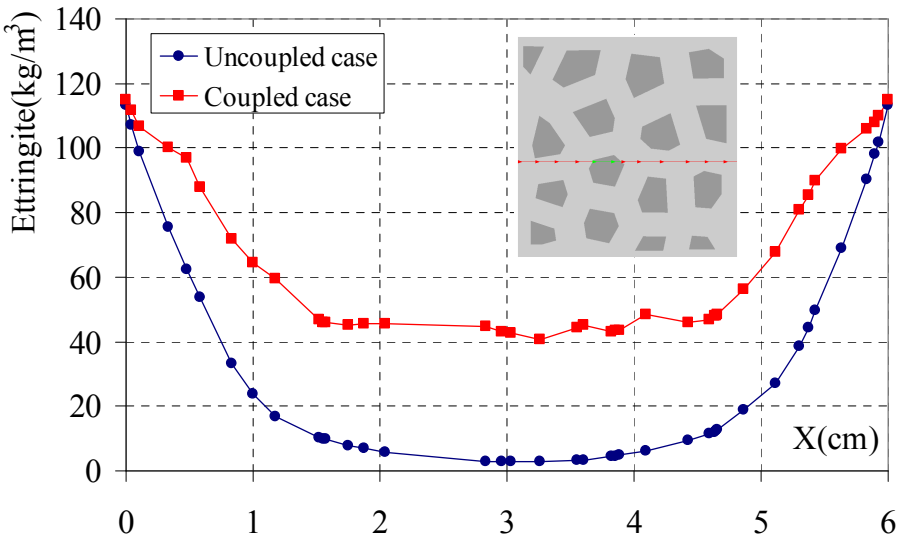

Figure 6.15. Ettringite concentration [kg/m^3] profiles at 2,572 days for the coupled and uncoupled analyses, at the specified cross-section of the mesh.

Note that in the coupled analysis the internal cracking is much more pronounced when passing from 1,522 to 2,022 days of exposure, and that from 2,022 to 2,572 days micro-cracking is propagated around all the aggregates in the sample, representing the total disaggregation between matrix and aggregate, while cracks through the matrix going between aggregates unload. The simulation captures the crack patterns and the spalling phenomena observed in lab experiments in a correct way, with the resulting reduction of effective area of the sample, and even the almost complete disintegration of the sample. This can be seen qualitatively in figure 6.16, in which the deformed mesh obtained with the simulation is compared to the final state of a real concrete sample (Al-Amoudi, 2002).

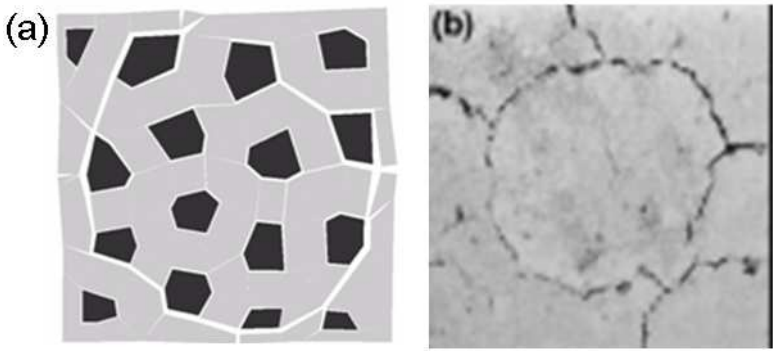

Figure 6.16. Qualitative comparison between numerical results and experimental observations: (a) deformed mesh and (b) real cracked specimen (from Al-Amoudi, 2002).

Another aspect observed in the simulations consists of the effect of introducing a porosity dependence of the diffusion coefficient for the sulfates ingress (eq. 6.14). The uncoupled analysis has shown a decrease of the sulfate concentration with time at a certain exposure period, which is caused by the pore clogging effect on the diffusivity. The initial diffusion coefficient adopted in the simulation is $D_0 = 1.96x10^{-12}$[m^2/s] = 0.0017[cm^2/day]. Figure 6.17 shows the diffusivity distribution of the matrix phase at 2,022 days of exposure, when the decrease of the sulfate concentration with time is at the onset. It may be observed that, due to the fact that the precipitation of ettringite has

its maximum near the exposed surfaces, an outer layer with clogged pores is formed, causing a considerable decrease of the diffusion coefficient (of 2.2 times in the figure), and therefore an important decrease of the sulfates supply.

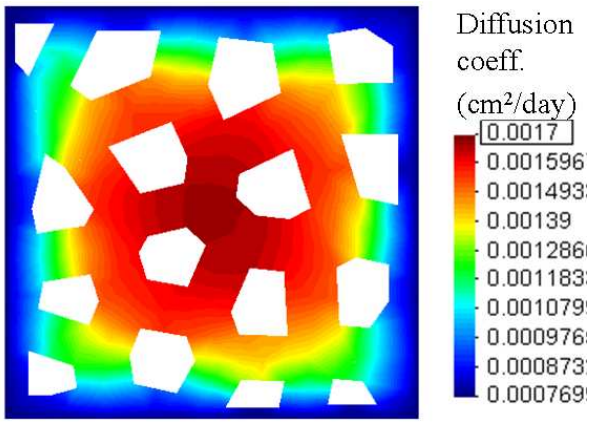

Figure 6.17. Distribution of the diffusion coefficient values in the matrix phase at 2,022 days of exposure: effect of the precipitation of ettringite on the reduction of porosity.

Due to this rather sharp decrease of the sulfates supply, the internal availability of sulfates is diminished in time due to the consumption in the ettringite formation reaction. This is plotted in figure 6.18, in which the profiles of sulfate content are shown for different exposure times. Figure 6.18a plots three profiles before the critical time at which sulfate concentration diminishes with time, showing, for any given value of the abscissa, increasing amounts of sulfates with time. On the other hand, after this critical time, which in the simulation is at around 1,000 days, this tendency is reversed and the amount of sulfates decreases in time at a given value of the abscissa, due to a greater consumption of sulfates in ettringite formation as compared to the increase due to diffusion, as shown in figure 6.18b.

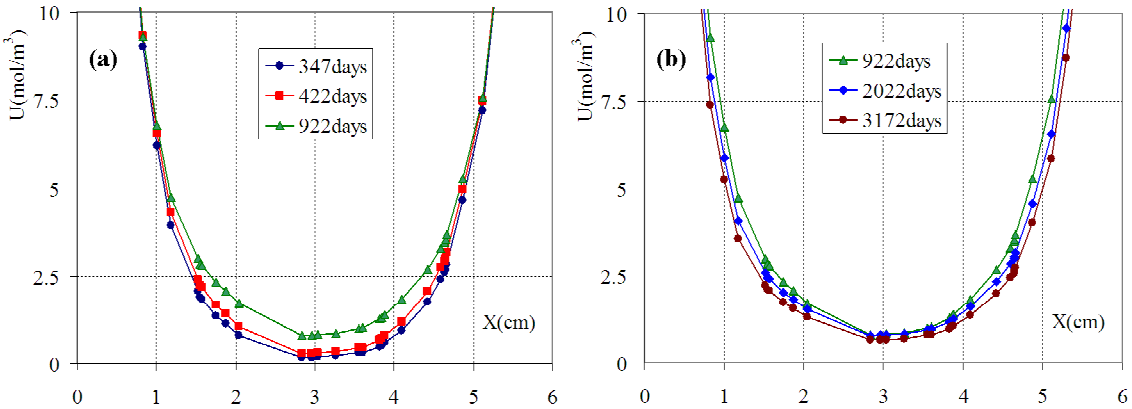

Figure 6.18. Profiles of the sulfate concentration [mol/m^3] for different exposure periods: (a) 347, 422 and 922 days, showing an increase of sulfate concentration in time; (b) 922, 2,022 and 3,172 days showing a decrease in the sulfate concentration.

This *a priori* unexpected behavior has not been found in the coupled simulations, in which the effect of cracking and spalling on the diffusion process is predominant. Accordingly, at the critical time at which the diffusion would be reversed (1,000 days), the crack formation in the coupled analysis allows for the penetration of sulfates through these preferential channels, thus yielding increasing amounts of sulfates.

It should be noticed that the present model does not account for the leaching process involving the dissolution of portlandite, which may not be generally decoupled from the sulfate attack problem, as discussed in the previous chapter (Le Bescop & Solet, 2006). The leaching process is typically accompanied by an increase in the porosity, which is not considered in the present model. Future work in this line should probably include this feature.

6.3.2. Influence of the initial C_3A content of the cement

In the previous chapter, the important influence of the C_3A content of the cement in the resistance of concrete to sulfate attack was pointed out. It is well-known that a low C_3A content minimizes the monosulfoaluminate content and therefore the potential formation of ettringite, leading to much more reduced expansions. Thus, as a second step, the influence of the C_3A content on the mechanical overall response has been studied with the same academic example of a $6x6cm^2$ concrete specimen, shown in figure 6.11. To this end, another coupled simulation, in addition to the one presented in the previous section (with 9.13% wt. of C_3A), has been performed considering a C_3A content of 4.56% wt., the rest of the parameters remaining identical to the previous example.

In order to derive the C_3A concentration [mol/m^3] of the matrix phase, representing mortar plus smaller aggregates, from the weight percentage in the cement (% wt.), the following transformation is used (Clifton & Pommersheim, 1994)

$$\mathrm{c}\left[\mathrm{g}/\mathrm{cm}^3\right] = \mathrm{p}\cdot v_c = \mathrm{p}\cdot\left(1+\frac{\rho_\mathrm{c}}{\rho_\mathrm{s}}\left(\frac{\mathrm{s}}{\mathrm{c}}\right)+\frac{\rho_\mathrm{c}}{\rho_\mathrm{w}}\left(\frac{\mathrm{w}}{\mathrm{c}}\right)\right)^{-1} \tag{6.33}$$

in which v_c [m^3/m^3 of material] is the volumetric fraction of cement in the concrete, p is the weight percentage of C_3A in the cement, $\rho_\mathrm{c}, \rho_\mathrm{s}, \rho_\mathrm{w}$ are respectively the densities of cement, aggregates and water, and s/c and w/c are the aggregate to cement and water to cement ratios, respectively (in weight). In order to calculate s, one has to deduct from the total amount of aggregates in the concrete, the fraction explicitly discretized in the mesh. Finally, a transformation with the molar weight M^{C_3A} (269.9 g/mol in the case of C_3A) is calculated as

$$\mathrm{C}[\mathrm{mol}/\mathrm{cm}^3] = \frac{\mathrm{c}[\mathrm{g}/\mathrm{cm}^3]}{\mathrm{M}^{C_3A}[\mathrm{g/mol}]} \tag{6.34}$$

The results obtained regarding the mechanical response for the low C_3A case are compared to the high C_3A one in figures 6.19 and 6.20. In figure 6.19, the energy spent in fracture processes is plotted for both cases at different exposure times, whereas in figure 6.20 the results are presented in terms of the deformed meshes. From both figures, it is evident that the low C_3A case has a much higher sulfate resistance than the latter, given by an important retardation of the spalling of the concrete outer layer, which occurs approximately 3 years later than the high C_3A content sample (from around 1,022 to 2,022 days). Note that also the interior of the sample remains relatively unaltered in the low C_3A case.

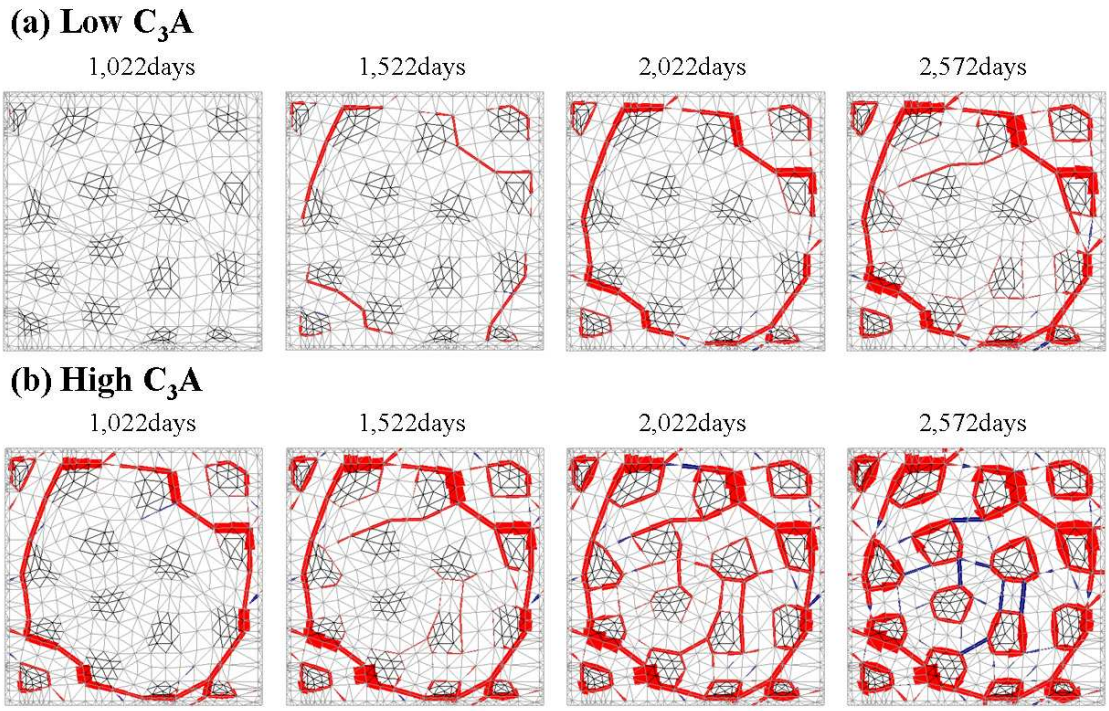

Figure 6.19. Comparison of the crack pattern evolution, in terms of the energy spent in fracture, between two cases with a (a) low and a (b) high C_3A initial content in the cement, for values of the exposure time of t = 1,022, 1,522, 2,022 and 2,572 days.

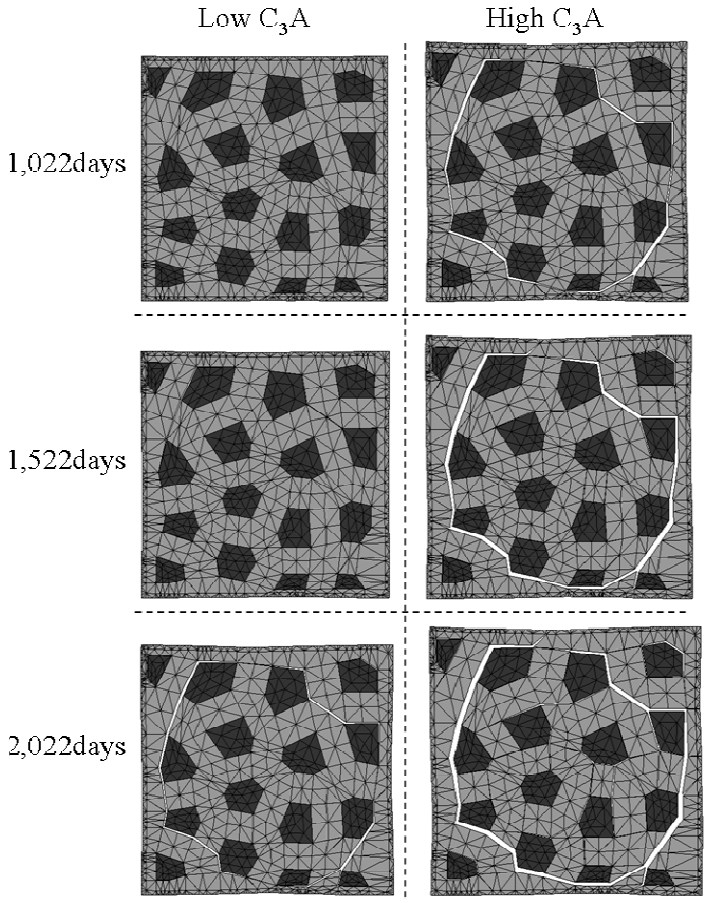

Figure 6.20. Comparison of the deformed meshes for the same cases as figure 6.11, for values of the exposure time of 1,022, 1,522, 2,022 and days.

The important differences observed between the two cases may be explained when plotting their equivalent aluminates phase (reacting with the ingressing sulfates) concentrations. First of all, equation 6.8 states that the rate of consumption of the aluminates phase (and thus the rate of formation of ettringite, see eq. 6.5) is proportional to its concentration. Therefore the expansions are expected to happen faster in the high C_3A content sample. This is shown in figure 6.21a,c, presenting the remaining CA profiles for both cases at 1,022 days (a) and 2,022 days (c), where a larger CA consumption may be observed in the high C_3A content sample. If these quantities are normalized with the initial CA concentration in each case, the differences are not very significant (figure 6.21b,d). What can be observed is that at 1,022 days of exposure the low C_3A sample has consumed relatively larger amount of CA. On the other hand, this tendency is slightly inverted for 2,022 days, showing again a higher rate of CA depletion in the high C_3A sample.

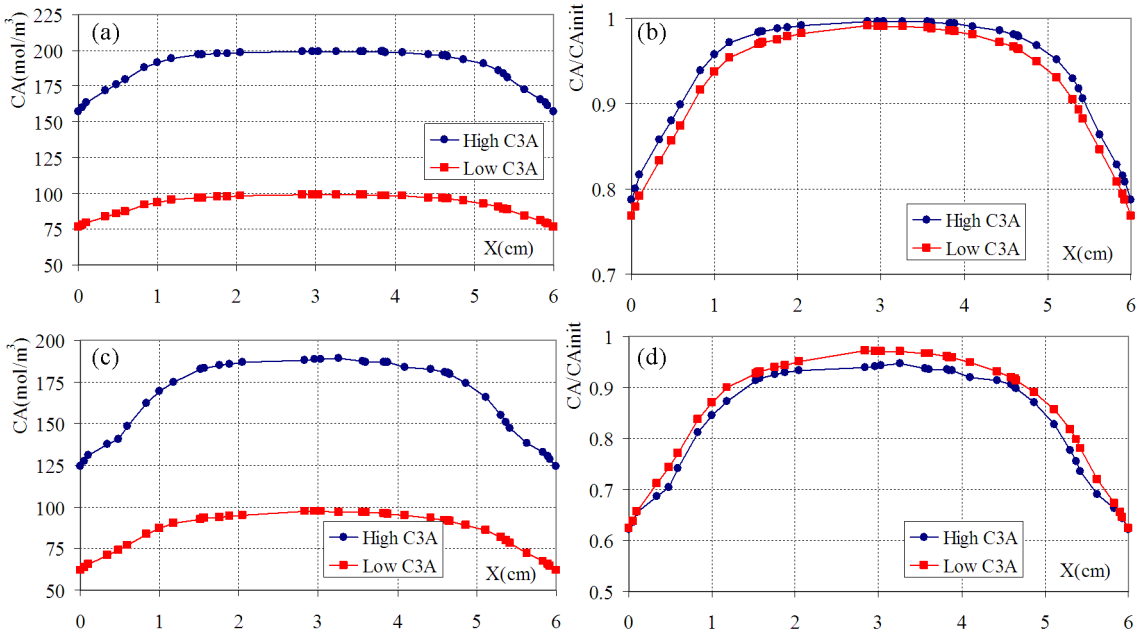

Figure 6.21. Comparison of the remaining equivalent CA concentration profiles for the low and high C_3A samples at the age of 1,022 (a,b) and 2,022 days (c,d). Absolute values (a,c) and normalized values with the initial concentration (b,d).

6.3.3. Influence of the diffusion through the cracks

In this section, the influence on the coupled behavior of concrete specimens of different relationships between the diffusion coefficient for interface elements and the crack opening is examined. The goal is to assess the sensitivity of the diffusivity on the crack width, and the impact on the overall diffusion process and mechanical response. Additional simulations of the same concrete specimen shown in figure 6.11 have been carried out considering first the validity of the cubic law with two different parameters (see figure 6.22a), and then with the introduction of a quadratic-linear law (see expressions 6.21 to 6.23) for the calculation of the diffusivity of the crack, as discussed in section 6.1.3.

Figure 6.22 plots the three different laws as a function of crack opening. The cubic law with two different parameters η ($1x10^5$[1/day], denoted as low, and $1x10^8$[1/day], denoted as high) yields a sharp increase of the diffusivity with the crack width. The case of the cubic law with a high parameter is equivalent to assume that one cracking has

started the diffusion through the cracks will be dominant, as opposed to that through the continuum. In the case of a low parameter, the relation behaves similarly to the quadratic-linear law until a crack opening of around 10 microns, after which the increase is much more pronounced in the former. It should be reminded that typical maximum crack openings in the simulations of external sulfate attack are in the order of 100 to 200 microns for the spalled layer, which are an order of magnitude larger than in the case of drying shrinkage, covering all the range plotted in figure 6.22.

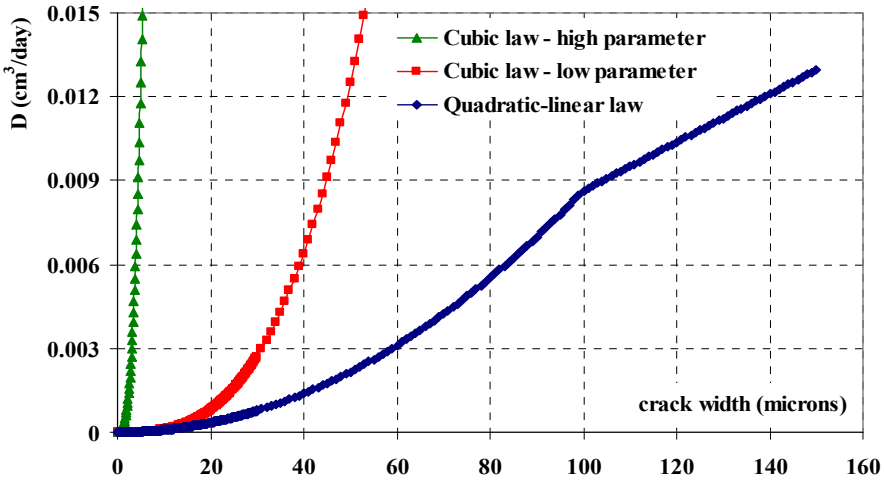

Figure 6.22. Comparison of three different relationships between diffusivity and width of the crack adopted: cubic law with two different parameters and quadratic-linear law.

First, the results of the two simulations assuming the cubic law with a low and a high parameter η, are presented in figures 6.23 to 6.25. Figure 6.23 depicts the sulfates distribution at three different exposure periods for the two cases. It can be clearly observed that as a direct consequence of the increase by 3 orders of magnitude in the parameter η, which yields a much higher diffusion coefficient through the crack, the diffusion of sulfate ions in the specimen is highly affected once cracking has started. On the other hand, the ettringite distribution, presented in figure 6.24, is less sensitive to this variable for the same exposure periods, although this is mainly due to a retardation effect caused by the consideration of reaction kinetics for ettringite precipitation. In figure 6.25, the crack patterns in terms of the energy spent in the fracture process for the same three exposure times are presented, showing appreciable differences, starting from around 1,500 days. At 1,801 days of exposure, the case with a high parameter η shows appreciable internal microcracking, which is not observed in the other case.

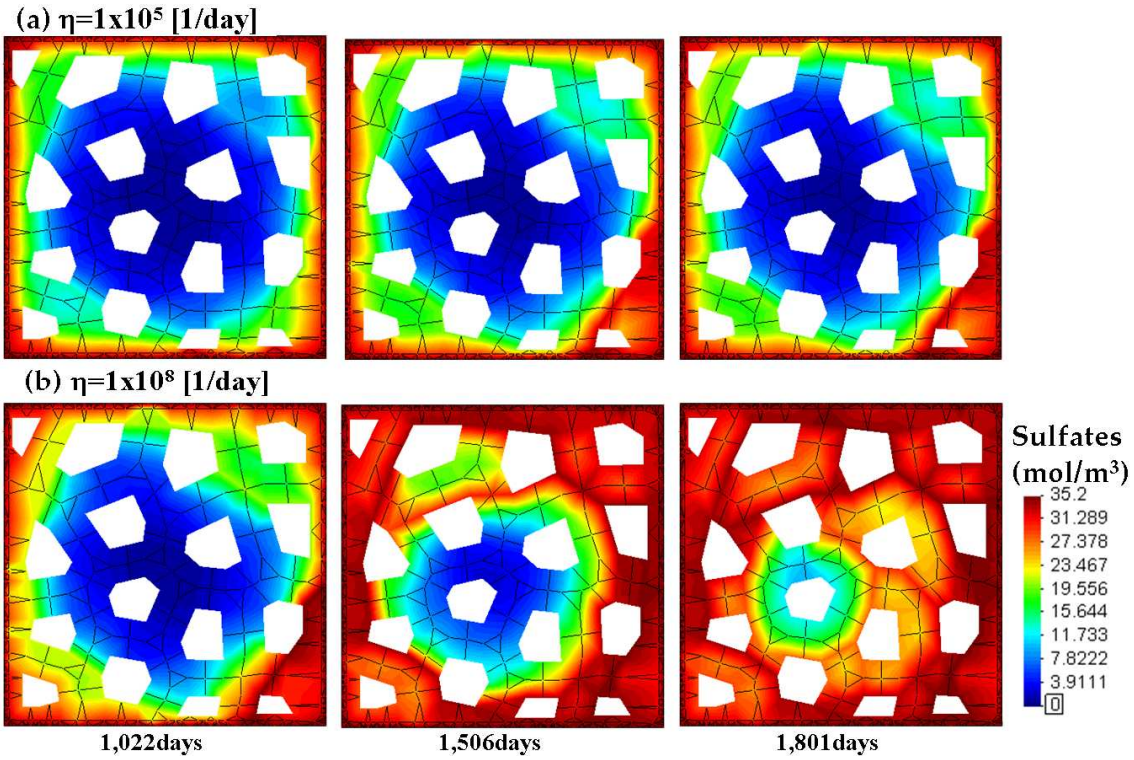

Figure 6.23. Sulfates distribution [mol/m^3] for three different times of exposure (1,022, 1,506 and 1,801 days), comparing the results obtained by assuming a (a) low and a (b) high value for the parameter in the cubic law.

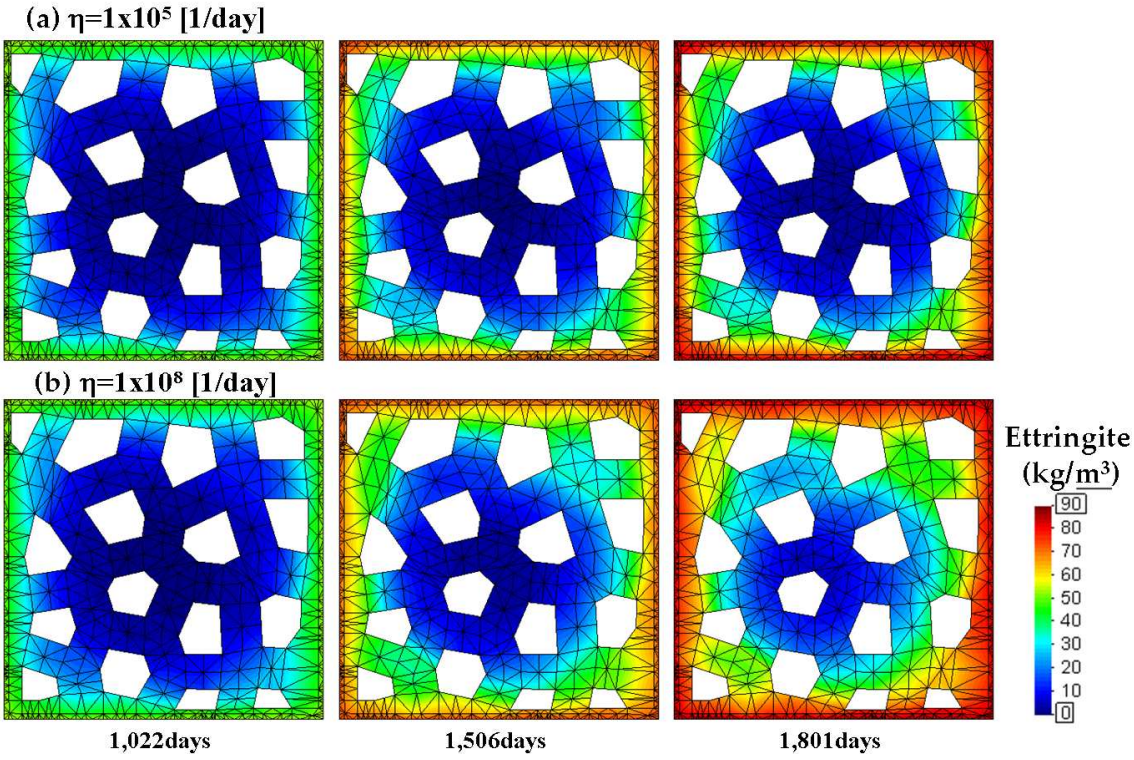

Figure 6.24. Ettringite distribution (kg/m^3) for three different times of exposure (1,022, 1,506 and 1,801 days), comparing the results obtained by assuming a (a) low and a (b) high value for the parameter in the cubic law.

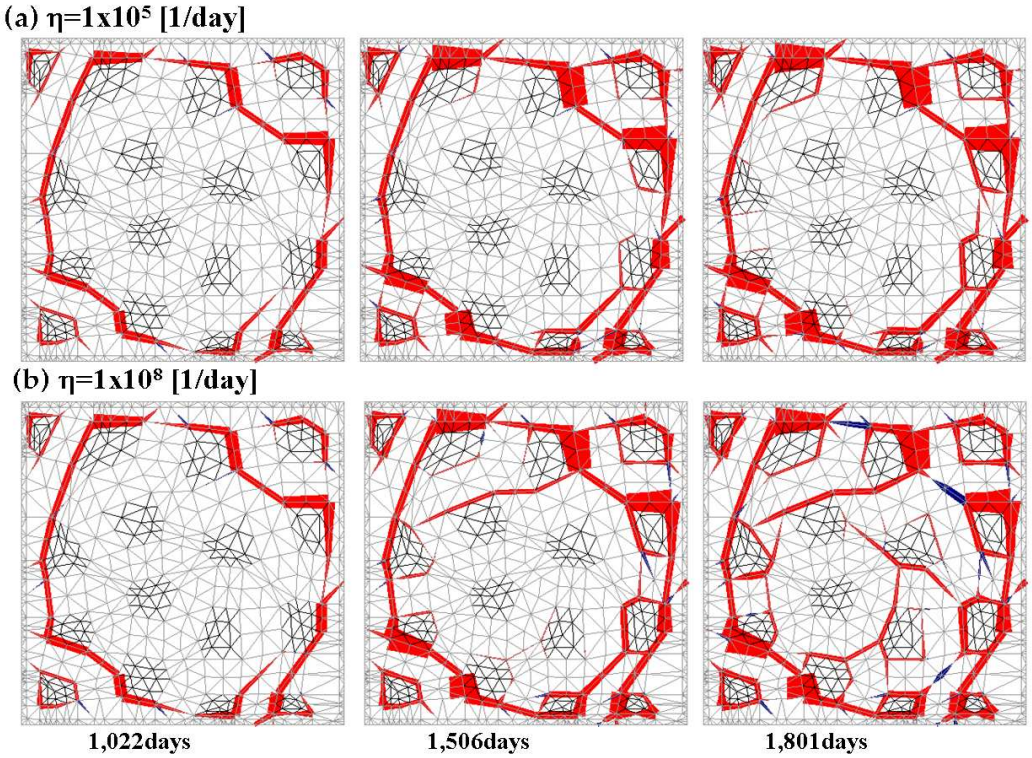

Figure 6.25. Crack patterns in terms of the energy spent in the fracture process for three different times of exposure (1,022, 1,506 and 1,801 days), comparing the results obtained by assuming a (a) low and a (b) high value for the parameter in the cubic law.

Next, the cases of assuming the cubic law with a low parameter and the quadratic-linear law (presented in section 6.1.3.) have been compared. In figure 6.26 the sulfates concentration for the same three exposure times as in figure 6.23 are presented for both cases. The differences found are much less pronounced than in the previous comparison, partially due to the similarity of both relationships until a crack opening of around 10 microns. At 1,506 days of exposure, the increase of the sulfates concentration in the case of adopting the cubic law with a low parameter becomes noticeable (see lower-right corner of the specimen). However, the crack patterns in both cases are similar, with a slightly higher level of internal microcracking in the case of using the cubic law, and only for advanced stages of the degradation process.

From the preceding simulations, it is clear that the resulting sulfates distribution at a certain exposure period is very sensitive to the relationship assumed between diffusivity and aperture of the cracks, and to a lesser extent, also the ettringite concentration distribution and crack patterns obtained. It may be concluded that considering the additional diffusion through the cracks is therefore important and cannot be generally disregarded. The case in which the cubic law with a high parameter is assumed would represent a limiting case, in which the cracks act as instantaneous penetration channels. The other two cases considered represent intermediate states between the former and an uncoupled simulation. If the recent experimental observations on the diffusion of chlorides ions (Djerbi *et al.*, 2008) are extrapolated to the case of sulfates and assumed to be valid, the cracks would only have a noticeable effect on the overall diffusion process at more advanced states of degradation, as compared to the results obtained with the cubic law.

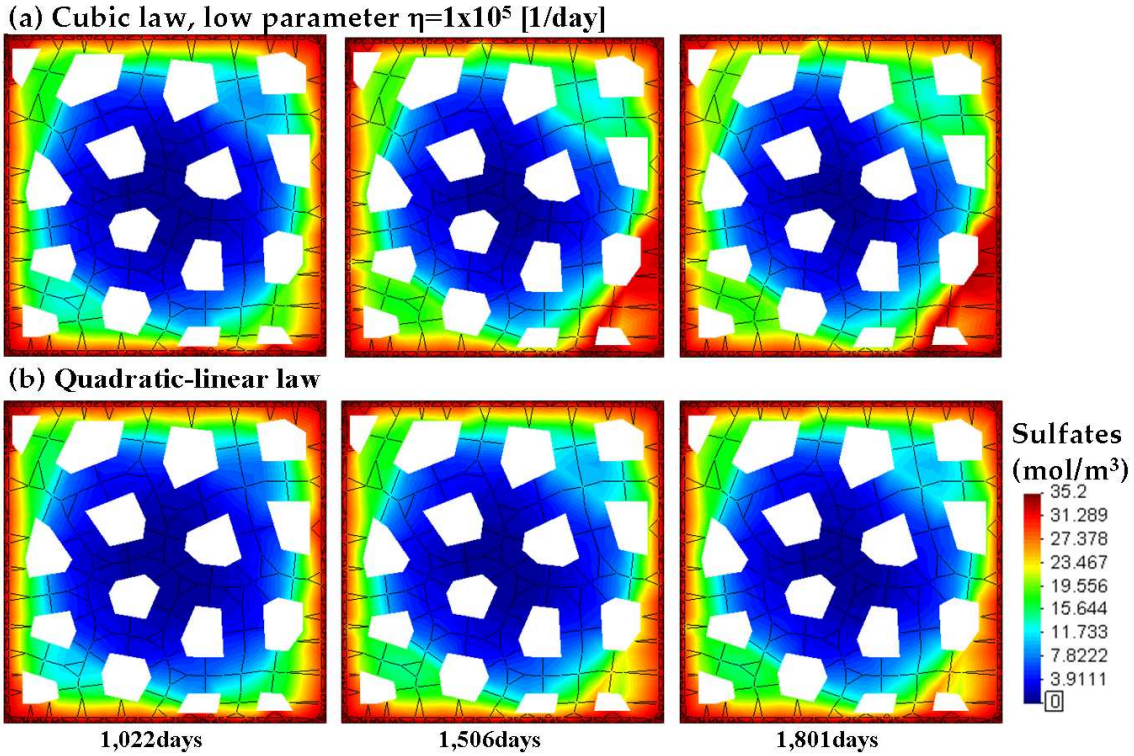

Figure 6.26. Sulfates distribution [mol/m^3] for three different exposure times (1,022, 1,506 and 1,801 days), comparing the results obtained assuming the (a) cubic law with a low parameter and the (b) quadratic-linear law for the diffusion through the cracks.

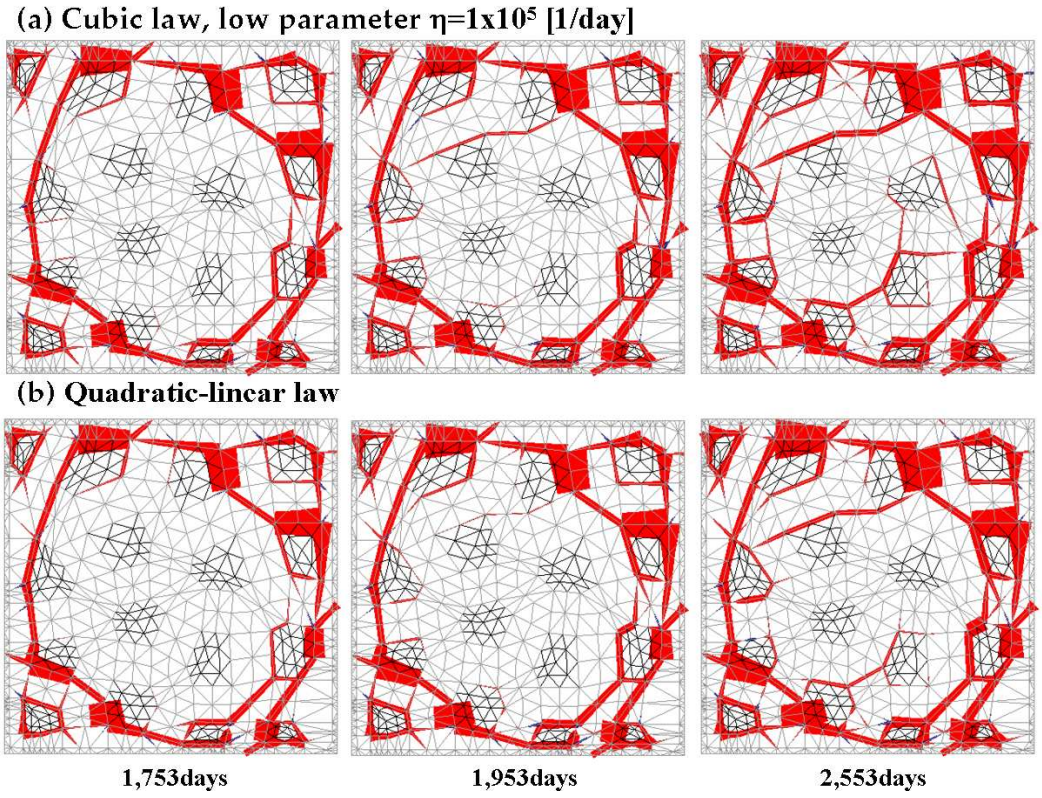

Figure 6.27. Crack patterns in terms of the energy spent in the fracture process for three different times of exposure (1,753, 1,953 and 1,2553 days), comparing the results obtained by assuming the (a) cubic law with a low parameter and the (b) quadratic-linear law for the diffusion through the cracks.

6.4. Simulation of the experiments by Wee *et al.* (2000)

This section presents, the results obtained with the present model concerning the simulation of recent experiments of external sodium sulfate attack on concrete prisms (Wee *et al.*, 2000). In that work, a wide range of cementitious materials including ordinary Portland concrete (OPC), blast-furnace slag, silica fume and sulfate resisting cements were studied. However, in the present thesis we only focus on OPC, for which the chemical reactions involved and the degradation processes are better understood, as discussed in the previous chapter. Unfortunately, due to the complexity of the experimental determination of ettringite profiles (see e.g. Wang, 1994), the results in that work are only presented in terms of expansions and flexural strength.

Concrete prisms of $100x100x400mm^3$ were casted with w/c ratios of 0.4 and 0.5 with different curing periods (7 and 28 days). Samples were immersed in 5% sodium sulfate solution (corresponding to a concentration of 35.2 $[mol/m^3]$) and expansions were measured for 224days (visual inspection was carried out until 364 days). It has been chosen here to simulate the case with 0.5 w/c ratio and 28 days curing period, since we are only interested in capturing the right trends and confirming that the model yields reasonable approximations. A more extensive experimental validation campaign has been left out of this thesis. The experimental data for the tested concrete is summarized in table 6.2. The maximum aggregate size used was 20mm for the coarse fraction and 5mm for the fines.

In order to avoid the influence of the casting direction (e.g. warping of the samples observed in some experiments, see Schmidt, 2007), expansions were measured on the side faces (and not on the casting direction surfaces). The measurement basis is 200mm and the average of 4 measurements for 2 prisms is considered in the plot.

w/c ratio	0.5	curing period (days)	28
sand/total aggregate vol. ratio	0.48	Na_2SO_4 conc. (mol/m^3)	35.2
cement (kg/m^3)	370	cement type	ASTM Type I
water (kg/m^3)	185	C3A content	8.60%
sand (kg/m^3)	854	C4AF content	9.40%
coarse aggregate (kg/m^3)	925	aggregate type	crushed granite
compressive strength (MPa)	51.1	max. aggr. size (mm)	20
flexural strength (MPa)	5.4	specific gravity of aggr.	2.65

Table 6.2. Summary of the composition and mechanical properties of the concrete, and sodium sulfate solution concentration of the simulated experiments (Wee *et al.*, 2000).

The meshes used in the simulations are shown in figure 6.28, with an aggregate volume fraction of 30% (maximum and minimum aggregate sizes: 16.5mm and 5mm, respectively), as deduced approximately from the mix-design data. One of the meshes has dimensions $10x40cm^2$, generated to calculate the longitudinal expansions, with two different measurement bases. Additionally, a cross-section of the prism has been considered (size is $10x10cm^2$) to follow its degradation, accounting for the corner effects. The parameters finally used in the coupled calculations are summarized in table 6.3.

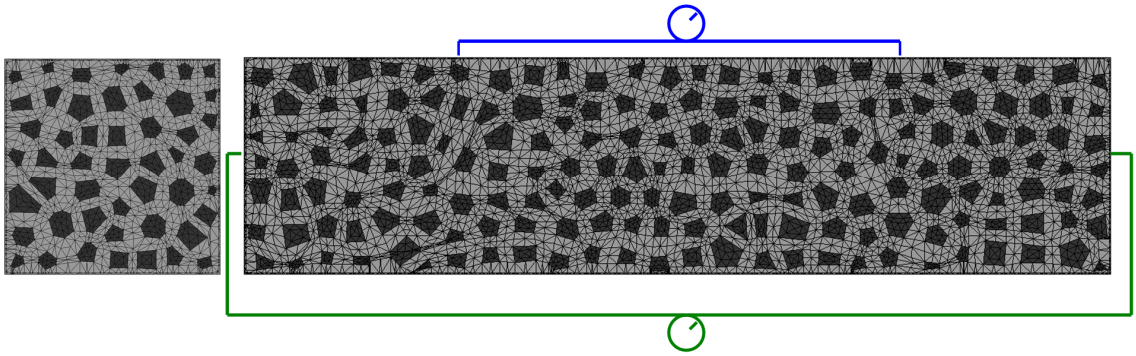

Figure 6.28. Meshes used in the simulations for the cross-section (size is $10x10cm^2$, left) and the longitudinal section (size is $10x40cm^2$, right) with different measurement bases.

Material parameters adopted			
Diffusion-reaction model (matrix)		Mechanical analysis (continuum)	
Initial humidity	100%	E_{matrix} (MPa, aging Maxwell chain)	26000 (at 28days)
D_0 (cm^2/day)	$0.24x10^{-2}$	E_{aggr} (MPa)	70000
D_1 (cm^2/day)	$1.2x10^{-2}$	ν_{matrix} ; ν_{aggr}	0.2 ; 0.2
β_D (–)	1.5	Mechanical analysis (interface elements)*	
k(m^3/(mol·day))	$1.5x10^{-4}$	χ (MPa)	2.5 ; 5.0
$\alpha_{hydration}$	0.90	c (MPa)	8.0 ; 16.0
w_0/c	0.50	$tan\ \phi$	0.7 ; 0.7
q	3	$tan\ \phi_{residual}$	0.2 ; 0.2
α_s	$1.133x10^{-4}$	GFI	0.04 ; 0.08
Diffusion analysis (interface elements)		GFIIa	10x GFI
η (1/day)	100.0x103	σ_{dil} (MPa)	40
Initial conditions		p_χ, p_c, p_{GF}	0.4, 0.5, 0.8
$CA_{initial}$(mol/m^3)	211.0	K_χ, K_c, K_{GF}	1.0, 1.0, 1.0
* values for aggregate-matrix and matrix-matrix joint elements			

Table 6.3. Summary of the material parameters used in the simulations of the experiments on concrete specimens by Wee and coworkers.

Figure 6.29 shows a qualitative comparison between the cross-section (end face) of a degraded OPC prism after 1 year of exposure and the deformed mesh (scale factor = 30) of the coupled simulation of the cross-section. In both cases, cracking is observed in the corners, although in the experiments the spalled layer is larger. This could be due to the fact that the photograph has been taken on the end face of the sample, where the degradation is maximal. This aspect cannot be considered in a two-dimensional simulation.

The expansions obtained in the simulation are compared with the experimental measurements in figure 6.30. Unfortunately, only a part of the degradation process has been analyzed at the moment. There is a small difference in the expansions measured with two different bases. The trend given by the blue line (measure 2), corresponding to the basis used in the experiments, seems to be correct, although calculations should be continued in order to verify the behavior at later stages.

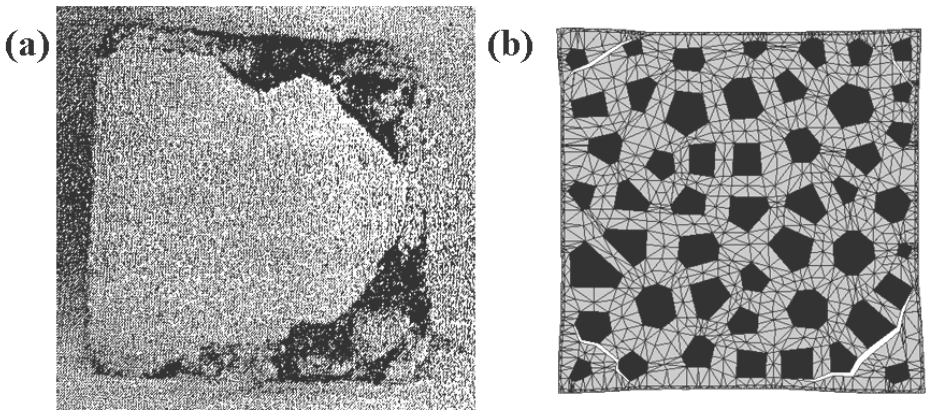

Figure 6.29. (a) Photograph of deteriorated concrete specimen of 0.5 w/c and cured for 7 days, after 52 weeks (364 days) of immersion (from Wee *et al.*, 2000). (b) Deformed mesh at 125 days of exposure (magnification factor = 30).

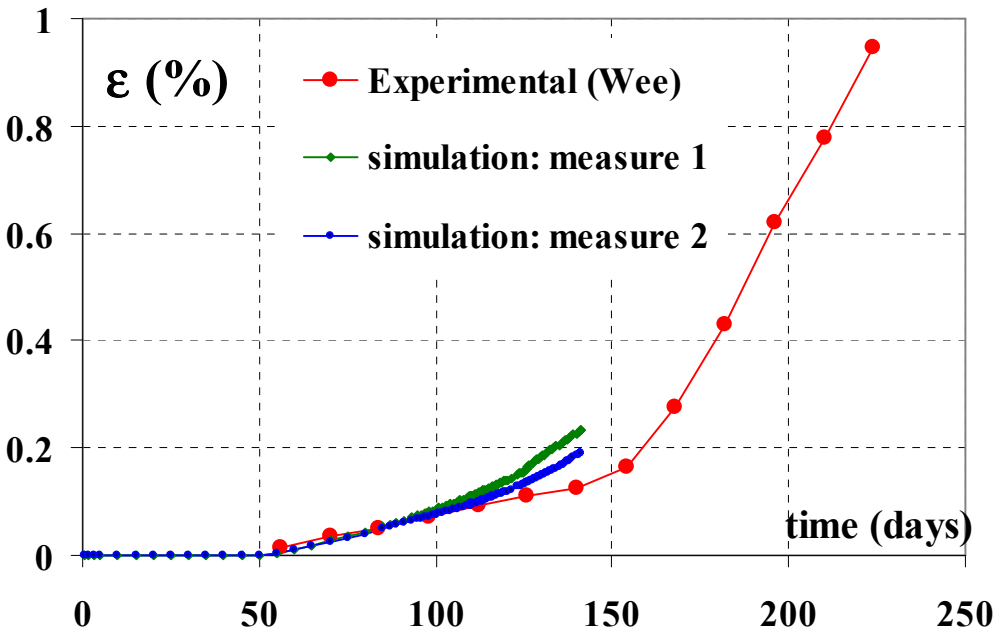

Figure 6.30. Longitudinal expansions as a function of time: comparison of experimental measurements and results of the simulation measuring strains at two different locations (measure 1 = between end faces; measure 2 = 200mm basis in the central part, average of both sides).

6.5. Partial conclusions on C-M modeling of external sulfate attack

A chemo-mechanical (C-M) coupled model for the analysis of external sulfate attack of saturated concrete specimens at the meso-level has been successfully developed and implemented. In this chapter, the formulation of the model has been presented in detail. The diffusion-reaction description is based on the work of Mobasher and coworkers (Tixier & Mobasher, 2003), with the addition of some refinements and the modification of specific features in the formulation. A simplified model that accounts for the main chemical reactions involved is considered. Precipitation of ettringite due to ingressing sulfates is assumed to be the cause of expansions. A threshold value for the volumetric change is introduced, below which there is a zero volumetric strain. The sulfate concentration is determined with the help of a diffusion-reaction differential equation

with second order kinetics for the consumption of sulfates and calcium aluminate phases. The diffusion coefficient for the uncracked continuous medium is considered to be a function of the capillary porosity, decreasing with the formation of ettringite, *via* a hyperbolic law.

Additionally, the effect of cracks on the diffusion process is explicitly taken into account with the introduction of zero-thickness interface elements, yielding an increase in the extent of the overall diffusion process. In this regard, three different cases have been analyzed, namely the assumption of the cubic law with two different parameters, and also assuming a quadratic-linear relationship derived from recent experiments on the diffusion of chloride ions (Djerbi *et al.*, 2008).

It has been shown that the model is able to represent the most important features of the mechanical response of concrete specimens under sulfate attack. The correct level of expansions at different exposure times, crack patterns around and between the aggregates, corner effects, and spalling of a matrix layer are well predicted by the model.

Numerical simulations presented in this chapter show that the effect of coupling is very important for a realistic representation of the diffusion process in the case of sulfate attack, in which the cracks play a fundamental role, and cannot be generally neglected. Indeed, when spalling occurs a drastic change in the boundary conditions for the diffusion of sulfates takes place, thus considerably accelerating the degradation process. Moreover, it has been shown that the extent of degradation may be sensitive to the relation assumed between the diffusivity of the crack and its aperture. Uncoupled analyses neglect this effect, predicting lower sulfate ingress at a given time. In fact, due to the pore filling effect on the diffusion coefficient through the uncracked porous medium, a reversal of the general trend of increasing sulfate concentration within the specimen has been detected in some of the uncoupled calculations, yielding lower amounts of ettringite formation than in the coupled cases, which did not show this feature. The maximum crack openings found in the simulations are in the order of 200μm, for the spalled matrix layer, which are an order of magnitude larger than in the case of drying shrinkage, explaining the relevance of accounting the effect of diffusion through the cracks.

The retardation of microcracking, fracture and spalling phenomena in concrete specimens with a low C_3A content, as compared to concrete made from regular cement, is qualitatively well predicted by the model. Moreover, macroscopic (homogeneous) simulations of mortar samples with a low C_3A content have resulted in a lower level of expansion than the high C_3A mortar. Finally, recent experiments on concrete prisms made with ordinary Portland cement (Wee *et al.*, 2000) have been simulated with the present model, yielding a reasonable approximation of the longitudinal expansions with time, at least during the first 140 days of exposure. However, calculations should be continued in order to verify the behavior at later stages.

Chapter 7

CLOSURE

In this thesis, the applicability of the finite element meso-mechanical model previously developed and applied to concrete specimens under purely mechanical loading within the same research group, has been extended to the analysis of hygro-mechanical and chemo-mechanical coupled problems, such as drying shrinkage and external sulfate attack in concrete. Cracking is introduced *via* zero-thickness interface elements equipped with an elasto-plastic constitutive law based on nonlinear Fracture Mechanics (NLFM), and the additional moisture diffusion through opened cracks is explicitly accounted for in the finite element simulation. The previous experience and tools developed within the group have served as basis for the work performed during the course of this thesis (López, 1999; Segura, 2007; Roncero, 1999; Caballero, 2005; Roa, 2004; López *et al.*, 2003; López *et al.*, 2005b). This work has led to a number of conclusions which are described in the following, together with a brief summary of the most relevant points. In addition, possible extensions of the model to other applications are discussed, and future research lines motivated by this work are outlined.

7.1. Summary and conclusions on the mesostructural modeling

The different various numerical models available for studying the mechanical behavior of concrete and other cementitious materials at the meso-level have been reviewed in some detail. They may be roughly grouped into three broad families: the lattice models, the particle models and the continuum models. While each model has its advantages and drawbacks regarding the representation of the geometries, the mechanical response, and their computational cost, continuum models seem the best suited for analyzing coupled problems at this scale and introducing explicitly the effect of cracks on the diffusion-driven phenomena. On the other hand, this feature is what makes the model presented here quite demanding computationally, since the systematic introduction of zero-thickness interface elements along all potential crack paths increases substantially the number of degrees of freedom.

Regarding the geometry generation, it has been emphasized that the methodology used in this thesis does not intend to explicitly represent the same aggregate size distribution as lattice and particle models. Instead, only the largest aggregates are generated through a Voronoï/Delaunay tessellation theory, and the surrounding matrix represents the homogenized behavior of mortar plus smaller aggregates. This is motivated by the fact that fracture and failure in concrete are generally governed by the main heterogeneities in the material.

It has been shown that the two-dimensional simulation of the mesostructure is a challenging task, not so much from the computational point of view (as is the case in 3D modeling), but in terms of the correct geometry representation. In this sense, it has been argued that with the help of stereology one can determine from a real 3D specimen the adequate section to be used in 2D. Stereology simply states that the volume fraction of inclusions is equal to the area fraction in a 2D section of the same composite. Unfortunately, a considerable number of sections may be required to be analyzed in order to determine the mean volume fraction and the standard deviation. This means that a random section of the composite will not, in general, have an area fraction equal or close to the volume fraction. In addition, two-dimensional simulations cannot capture the nonlinear three dimensional effects as bridging and branching of cracks in the out-of-plane direction and consequently they predict an overly brittle behavior. These issues make the interpretation of the quantitative analysis of concrete from 2D simulations quite challenging.

Regarding the constitutive modeling for zero-thickness interface elements, the work performed during this thesis has focused on enhancing the convergence of the integration algorithm by means of small refinements in the plastic potential of the original model (Carol *et al.*, 1997). Moreover, the constitutive law accounting for aging has been implemented within an existing numerical framework, with a backward-Euler integration scheme and a consistent tangent operator.

The structured mesh generation procedure has been described, pointing out some specific features which have been introduced in this thesis. The work done along this line has been focused on a greater control of the aggregate shape, post-processing aspects such as statistic representation of the geometry and results in terms of polar diagrams, the generation of an external frame for obtaining "cast" meso-geometries (meshes with an external matrix layer), the introduction of an automatic procedure for refining specific edges that will be exposed to diffusion-driven phenomena, and a procedure for the generation of notches of any desired size.

An integral approach for the meso-mechanical analysis has been presented, which combines a mesostructural representation of the main heterogeneities with the simulation of cracks *via* zero-thickness interface elements that account for the aging effect also including an aging visco-elastic behavior for the matrix phase.

7.2. Summary and conclusions on the drying shrinkage of concrete and its hygro-mechanical simulation

In order to gain insight on the essential features of drying shrinkage in concrete and to identify the main directions to be followed during this work, an exhaustive and critical review of the experimental evidence and the up-to-date available modeling tools has been carried out. Emphasis is made on the potential applicability of the present model, such as the study of the drying-induced microcracking and of the influence of aggregates in this process, the effect of cracks on the diffusion process or the consideration of different relations between weight losses and strains, among others.

The numerical results obtained and the main findings along this line have been presented and discussed in Chapter 4. In the following, the most relevant aspects are outlined:

- The coupled hygro-mechanical model at the meso-level presented in this thesis is able to satisfactorily represent the essential features of drying

shrinkage in concrete, such as the non-uniform moisture distribution due to the presence of aggregates and cracks, strains *vs.* weight loss relationship, stress profiles and crack patterns.

- The simulations have shown that the result of the effect of coupling is a slight increase in the drying state, but remains small in most practical cases. In fact, the difference could as well be considered to fall within the range of scatter of experimental results. The effect of coupling is only noticeable at the beginning of the drying process, when the drying through surface microcracks (of maximum crack openings) is most important. This is an important conclusion: in many cases uncoupled analyses can be performed without major loss of consistency of the obtained results and with significant reduction of computational cost.
- The effect of aggregates on the drying-induced microcracking has been extensively studied and qualitatively compared with experimental findings (Bisschop, 2002; Hsu, 1963; Mc Creath *et al.*, 1969). The performance of the model in this regard has proven satisfactory in most cases, even though some experimental evidence could not be totally reproduced, namely the effect of the aggregate size for a constant volume fraction: although the right trends in terms of crack front depth, polar diagrams and aspect ratios are well captured in this case, the differences between each case are not as significant, from a quantitative point of view, as in the experiments. It has been suggested that these differences could be attributed to the inherent deficiencies of a two-dimensional representation, as discussed in section 7.1.
- The model parameters have been adjusted to existing experimental results of concrete specimens (Granger, 1996), and the resulting numerical predictions have been found to agree well with experimental measurements. In addition, it has been shown that the consideration of a nonlinear local relationship between shrinkage strains and weight losses can be more accurate for simulating drying shrinkage experiments than the commonly employed linear relationship. Results have also hinted at the need for introducing a constitutive law for zero-thickness interface elements that accounts for the crack closure effect. Moreover, it has been found that considering the moisture capacity matrix as the derivative of the desorption isotherm does not have a considerable effect on the overall response, at least in the simulated cases, even though it is more consistent from a theoretical point of view.
- Finally, moisture diffusion has also been considered under mechanical loading. Preliminary analyses have confirmed that the well-known Pickett effect, or drying creep, cannot be solely attributed to the skin microcracking effect. It is concluded that the proposed model in its present form may be inappropriate to study drying creep experiments. The latter would require the introduction of an additional intrinsic mechanism, as briefly discussed in Chapter 3.

7.3. Summary and conclusions on the external sulfate attack and in concrete and its chemo-mechanical simulation

The numerical simulation of external sulfate attack in concrete is still not common in concrete mechanics and relatively few models exist up to date. Thus, it seemed

appropriate to make an overview of the fundamentals of the external sulfate attack problem in the light of experimental evidence available in the literature, in order to recognize the most relevant characteristics from the experimental point of view and to establish the desired features to be considered in the model. It is evident from this review that a complete treatment of the problem should involve chemical as well as mechanical aspects of sulfate ingress and their consequences in the overall behavior. Ettringite is believed to be the key factor behind expansions, although a number of proposed mechanisms coexist in the literature to explain expansion and degradation.

Secondly, a critical review of the existing models has been carried out. All existing models identified in the review treat the material as a continuous and homogeneous medium, and some of them propose a more detailed representation of the chemical reactions. The common feature is the phenomenological treatment of expansions as a result of the formation of reaction products (ettringite and/or gypsum). Only the recent model by Bary (2008) is capable of performing fully two-dimensional coupled analyses in a FE environment. But even this model lacks an explicit dependence of the transport processes on damage or cracking level. The rest of the models consider a variety of techniques to extract expansions or degradation profiles from 1D calculations. Moreover, none of them are able to capture the main crack patterns correctly, nor are they able to account for the effect that crack and spalling may have on the transport processes. Instead, only some of these propose an arbitrary increase in the diffusivity as a function of damage. It has been shown in this work that this is an important issue, since in the cases where spalling occurs, a drastic change in the boundary conditions of the chemo-transport analysis takes place, thus accelerating the degradation process.

A model for the analysis of external sulfate attack in concrete specimens has been successfully developed and verified. A chemo-transport model based on the work by Mobasher and coworkers (Tixier & Mobasher, 2003) has been implemented into the FE code DRAFLOW, using the mesostructural framework presented in this work. New features have been added to the original proposal, as the explicit diffusion through open cracks, the possibility of considering different kinetics for each chemical reaction, or the dependence of the diffusion coefficient of the uncracked continuum media on the capillary porosity (based on an hyperbolic law), which decreases due to ettringite precipitation in the pores. Moreover, the calculation of the volumetric expansions has been critically discussed and an alternative physical interpretation based on recent experimental observations has been suggested.

The simulations of external sulfate attack performed in this thesis have been presented in Chapter 6. The main results obtained and the conclusions drawn are summarized in the following:

- The effect of a single circular inclusion embedded in a matrix subjected to a uniform expansion has been analyzed numerically. The dependence of the aggregate-matrix crack width on the size of the aggregate has been compared to the analytical solution provided by elasticity theory, showing a very good approximation.
- An academic example of a $6x6cm^2$ concrete sample has been chosen for the evaluation of the coupled behavior of the model. It has been shown that the effect of coupling is very important in the case of external sulfate attack, due in part to the magnitude of the maximum crack widths found in the spalled layer, which are of the order of 100 to 200 microns (roughly an order of magnitude higher than in the case of drying shrinkage microcracks). Cracks

represent preferential penetration channels for the diffusion of sulfates into the sample. In turn, the acceleration of the diffusion-reaction process leads to a higher degree of mechanical degradation, with wider cracks around and between the aggregates, eventually leading to the disintegration of the sample. As a consequence, the penetration of sulfate ions is much more pronounced than in the uncoupled analysis.

- The effect of the C_3A content in the cement has been studied macroscopically in mortar samples and also at the mesoscale for the case of concrete. The results show lower levels of expansion on mortar prisms, as determined experimentally, and an important retardation of the cracking process in the low C_3A concrete specimen as compared to the high C_3A content sample, suggesting a much higher resistance to external sulfate attack in the former case.

- The sensitivity of the overall behavior on the diffusion through the cracks has been examined by comparing the results of three simulations at the meso-level of the same sample, but considering three different relations between diffusivity and crack opening, two of them based on the traditional cubic law with different parameters and one on the quadratic-linear law based on recent chloride diffusion experiments. As it could be expected, the sulfate attack is more severe as the diffusion through the cracks is increased. The cubic law, with two different parameters, has been compared with a quadratic-linear law based on recent experimental findings. The cubic law with higher parameter values seems to yield much more pronounced penetration of sulfates than the same law with lower values, but the latter does not differ too significantly from the quadratic-linear. More research is needed in this field to establish the correct relation between diffusivity through the discontinuity and the crack opening.

- Finally, recent experiments on concrete prisms subjected to a sodium sulfate solution (Wee *et al.*, 2000) have been simulated with the present model showing a reasonable approximation of the longitudinal expansions during the first 140 days of exposure. The calculations should be nevertheless continued in order to confirm the expansion measurements at later states of degradation.

7.4. Future research lines

During the course of this thesis, a number of different topics related to the research developed herein have arisen as possible future research lines, which in some cases have not been pursued due to the natural time constraints of any research project. Moreover, the reasonable success of the coupled analysis in 2D of the drying shrinkage and external sulfate attack as carried out in this thesis, allows envisaging new possible applications in the future. The most relevant topics and future directions are the following:

- The results of the hygro-mechanical simulations of moisture diffusion under mechanical loading have shown the need to consider an intrinsic mechanism relating moisture conditions and mechanical stresses at the constitutive level in these cases. Thus, the enhancement of the model formulation to enable the simulation of drying creep in concrete is one of the most important research

topics that should be addressed.

- The need for extending the analysis to the 3D case has been put into evidence. Its consideration would enable a consistent simulation of cylindrical specimens, which are often used in the experiments, and would allow the representation of any type of boundary conditions. It should also be noted that the limitations arising from the consideration of a 2D representation of geometries can only be totally overcome with a full 3D diffusion/mechanical analysis.
- In this first version of the model, the aging effect is decoupled from the moisture diffusion analysis, which is in fact a simplification of the real behavior. It is well-known that appropriate moisture conditions have to be present for aging to occur (dried materials will in general show very little increase in mechanical properties with time). A future version of the model should definitely include this effect, as proposed in other existing models (Bazant & Najjar, 1972; Cervera *et al.*, 1999).
- Results of the drying shrinkage simulations have underlined the need of introducing a new constitutive law for zero-thickness interface elements that accounts for the crack closure effect. In this connection, the development of a new constitutive model based on a damage-plasticity-contact formulation which at the same time retains the essential features of the present model, would be an important contribution. This challenging topic has been recently undertaken and is at present under development.
- New applications of the hygro-mechanical model could be sought, as the classical restrained shrinkage test or the study of shrinkage induced cracking in cement concrete overlays (Bolander & Berton, 2004).
- In the case of external sulfate attack, warping in prismatic specimens of $1x4x16cm^3$ exposed to sodium sulfate solutions observed in recent experiments (Schmidt, 2007) is a test case where the model could provide new insight.
- The coupled model implemented for studying the external sulfate attack in concrete has left some open topics for future improvements. In this study, the coupling with leaching has not been pursued. Thus, the increase in porosity due to portlandite dissolution is not considered in the present model. In order to introduce this effect, a multi-ionic diffusion-reaction model should be implemented (Bary, 2008; Marchand *et al.*, 2002). Another simplification in this first version is the fact that the elastic modulus of the continuum matrix phase is unaffected by the chemical degradation process. In order to account for this effect, a damage model (with the consequent regularization problems) or a homogenized scheme for the variable mechanical properties of the matrix should be implemented. Finally, the possibility of coupling the transport-mechanical model with an existing code for thermodynamic modeling of phase assemblage at equilibrium could be explored.
- A useful feature for coupled chemo-mechanical analyses would be the implementation of prescribed relative displacements in the interface elements, which could be generated as a consequence of the coupling to the chemo-transport process, in order to simulate the growth and formation of reaction products within the cracks and its effect on the overall dimensional stability

of the material.

- The improvements introduced in the mesh generation process during this thesis enable the simulation of more complicated geometries and different special tests and benchmarks; for instance the wedge splitting test, the Nooru-Mohamed mixed mode tests (on-going work, see Rodríguez *et al.*, 2009), the L-shaped specimen benchmark and the Willam's test at the meso-level. Some of this work is currently on-going within the research group.
- Finally, given the satisfactory performance of the mesostructural model in coupled problems, novel possible applications involving the introduction of new types of couplings and different coupling sources are envisaged, such as the thermo-hygro-mechanical (T-H-M) modeling of concrete at high temperatures (on-going work), and the chemo-mechanical (C-M) degradation processes due to alkali-silica reaction and delayed ettringite formation.